XROTOR

X-shaped Radical Offshore Wind Turbine for Overall Cost of Energy Reduction

D5.2

Scaled rotatory transformer models, design and control

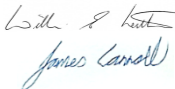🌐 **https://xrotor-project.eu**

🐦 **@XROTORProject**

December 2022

Document Information

Deliverable ID	5.2
Deliverable Title	Scaled rotatory transformer models, design and control
Lead beneficiary	University of Strathclyde
Contributing beneficiaries	
Due date Annex I	2022.12.21
Issue date	2022.12.21
Dissemination level	Public
Author(s)	Reza Yazdanpanah, Seyed Mortazavizadeh, David Campos-Gaona, Olimpo Anaya-Lara.

Approval

Version	Date	Description	Reviewed by	Approved by
1	2022.12.21	First release	Bill Leithead & James Carroll	Bill Leithead

XROTOR Consortium

University of Strathclyde

Delft University of Technology

University College Cork – National University of Ireland, Cork

Fundacion Cener

General Electric Renovables España

Norwegian University of Science and Technology

https://xrotor-project.eu

Table of Contents

About XROTOR

XROTOR: "X-shaped Radical Offshore wind Turbine for Overall cost of energy Reduction" is a Horizon 2020 funded project which aims to develop a disruptive new offshore wind turbine concept.

The XROTOR project is led by University of Strathclyde (UK) in partnership with Norwegian University of Science and Technology (Norway), Delft University of Technology (Netherlands), University College Cork (Ireland), Fundacion Cener National Renewable Energy Centre (Spain) and GE Renovables España (Spain).

As the effects of climate change are becoming ever more visible, Europe has raised its target for the amount of energy it consumes from renewable sources from the previous goal of 27% to 32% by 2030. Offshore wind energy can play a key role in achieving the EU target and contribute to the required 40% reduction in CO_2 emissions. However, to achieve the previously mentioned targets the cost of offshore wind must be reduced. The XROTOR concept provides a direct route to drastically reducing both capital and operating costs of energy from offshore wind.

The project runs for three years from January 2021, during which time, the concept will be developed through a holistic consideration of technical, cost, environmental and socio-economic impact aspects.

If proven feasible, XROTOR will, as a disruptive new offshore wind turbine concept, create new opportunities for the European wind energy industry and play an important role maintaining the EU's position as global technological leader in renewable energy, reducing greenhouse gas emissions and decarbonising the EU economy.

For more information see **https://xrotor-project.eu**

Description of the deliverable and its purpose

This report presents the design of a rotary transformer configuration (i.e. a wireless power transfer system) capable to handle the MW power transfer requirement of the XROTOR system. The deliverable includes a detailed specification of the rotatory transformer including parameters such as operating frequencies, current density, windings area, air-gap length, and others. The efficiency is quantified using finite element simulation and numerical calculations. Furthermore, its thermal performance at rated power levels is analysed and quantified using finite element simulation. The simulation results show that high level of efficiency (around 98.5%) can be obtained with a proper design methodology and suitable compensation network for the transformer system.

The second section of the report provides the design and analysis of a suitable power electronic topology for the rotary transformer to manipulate the wireless power flow at the levels of efficiency required by the XROTOR project. The analysis includes electrical operation and energy conversion losses simulation of a three-phase dual active bridge configuration suitable for high-power wireless power applications. The simulation demonstrates the suitability of the topology to drive MW level power through a rotary transformer system at efficiencies of around 98%. This efficiency is calculated via electrical and thermal analysis and simulations.

Results indicate that the combined efficiency of the rotary transformer with its associated power electronic converter turned to be 96.53% for a 1MW system.

The methodologies presented in this deliverable can be utilized to design multi-MW level rotary transformer system and associated power electronic drivers. The designed parameters utilize the standard DC voltage levels of commercial back-to-Back converter for wind generators. As such, the designs presented in this report can be incorporated as another energy conversion stage in the DC bus of a commercial Back-to-Back power electronic system.

List of acronyms

ΔΔ	Delta to delta
3P-DAB	Three phase dual active bridge
AC	Alternating Current
AWG	American Wire Gauge
BJT	Bipolar junction transistor
DAB	Dual-Active-Bridge
DC	Direct current
FEA	Finite Element Analysis
IGBT	Insulated-gate bipolar transistor
MCR-WPT	Magnetically coupled resonant wireless power transmission
MEC	Magnetic equivalent circuit
MMF	Magneto motive Force
MOSFET	Metal–oxide–semiconductor field-effect transistor
MW	Mega watt
PP	Parallel-Parallel
PS	Parallel-Series
PTE	Power transfer efficiency
RMS	Root mean square
RT	Rotary transformers
SP	Series-Parallel
SS	Series-Series
VA	Voltampere
VAWT	Vertical-axis wind turbine
YY	Wye to wye
ZVS	Zero-Voltage Switching

1   Introduction

The XROTOR is a novel hybrid wind turbine concept that retains some of the advantages of a vertical-axis wind turbine (VAWT) [1, 2]. As depicted in Figure 1, the XROTOR concept has a primary vertical axis rotor consisting of an upper and lower part with relatively conventional blades that are angled both upwards and downwards from the ends of a relatively short, stiff cross-arm. The role of the upper part is to provide the major contribution to mechanical power extraction from the wind. Secondary horizontal axis rotors are attached to the lower blades of the primary rotor, which extract wind energy. This design reduces the overturning moment on the main bearing and reduces the size and weight of the rotor, thus saving on the cost of maintenance and installation. Furthermore, it can capture more energy from the wind, which greatly improves the efficiency of the machine.

In the conventional vertical axis wind turbine, the vertical axis rotor plays a role in power take-off. However, in the XROTOR, the aerodynamic torque on the primary rotor is not balanced by the reaction torque from a generator. Instead, it is balanced by the thrust on the secondary rotors. As such, the energy conversion is carried out entirely by the generators of the secondary rotors. Given the high speed of rotation of the secondary rotors, their size can be reduced. This approach can simplify the power-take-off system and reduce the weight of the wind turbine. Since the energy conversion is carried out entirely in the secondary rotor, the challenge of transmitting energy from a rotating structure to the turbine's tower needs to be addressed.

Figure 1 The XROTOR Offshore wind turbine concept.

1.1   *The problem of using slip rings in offshore wind turbines.*

The traditional slip ring technology with an electric brush is mature and widely used in the industry. Whether it is the application of a rotary joint or the application of a rotating assembly platform, the slip ring plays a vital role in providing rotary systems power transmission and signal transmission; however, due to the friction between the brush and the contactors of the slip rings, its operation produces ageing and wear of the brush, which is reflected in maintenance cost. Furthermore, the accumulation of conductive particles (a product of the slip ring wear-out) increases the short circuit risk, including spark discharge, local overheating, abnormal noise, and effects on power quality. Rings approaching a slightly acute brush angle can result in

"friction chatter", which cause mechanical damage to the brushes or loss of brush contact resulting in arcing [3].

Under normal conditions, metal transferred from the rings to the brush is vaporized, forming the lubricating film. When metal from the rings does not totally vaporize, the metal particles imbed into the porosity of the brush surfaces, this increases slip ring wear and requires increased maintenance. Finally, electric currents also affect the wear of individual brushes; the higher the current, the faster the wearing which causes unnecessary shutdowns to change the individual short brushes [4].

With regards to the offshore use of slip rings, a detailed comparison of failure rates of offshore wind turbine under various conditions was carried out in [5] and is shown in Figure 2. The first three sub-components that cause failures are the pitch/hydraulic system, other components, and the generators. The generator mode failures are presented in Figure 3 which shows that slip ring problems are the most significant cause of generator failures, accounting for about 31% of all failures in this area. The failure rates of the remaining four problems are all less than 12%, which include bearing problems, generator grease pipe problems, rotor, and fan replacement problems.
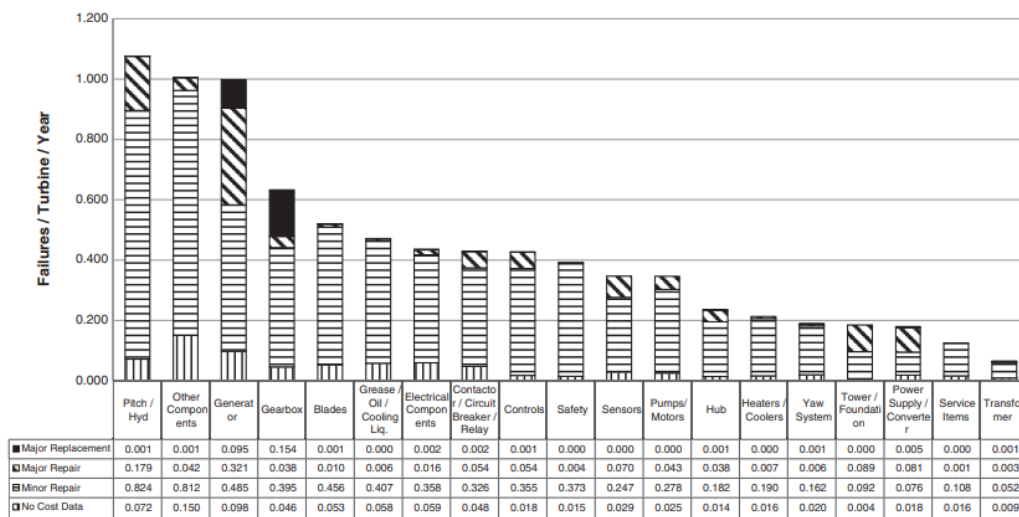

	Pitch / Hyd	Other Compon ents	Generat or	Gearbox	Blades	Grease / Oil / Cooling Liq.	Electrical Compon ents	Contacto r / Circuit Breaker / Relay	Controls	Safety	Sensors	Pumps/ Motors	Hub	Heaters / Coolers	Yaw System	Tower / Foundati on	Power Supply / Converte r	Service Items	Transfor mer
■ Major Replacement	0.001	0.001	0.095	0.154	0.001	0.000	0.002	0.002	0.001	0.000	0.000	0.000	0.001	0.000	0.001	0.000	0.005	0.000	0.001
▨ Major Repair	0.179	0.042	0.321	0.038	0.010	0.006	0.016	0.054	0.054	0.004	0.070	0.043	0.038	0.007	0.006	0.089	0.081	0.001	0.003
▤ Minor Repair	0.824	0.812	0.485	0.395	0.456	0.407	0.358	0.326	0.355	0.373	0.247	0.278	0.182	0.190	0.162	0.092	0.076	0.108	0.052
▯ No Cost Data	0.072	0.150	0.098	0.046	0.053	0.058	0.059	0.048	0.018	0.015	0.029	0.025	0.014	0.016	0.020	0.004	0.018	0.016	0.009

Figure 2 Failure rate Pareto chart for subassembly and cost category of wind farms

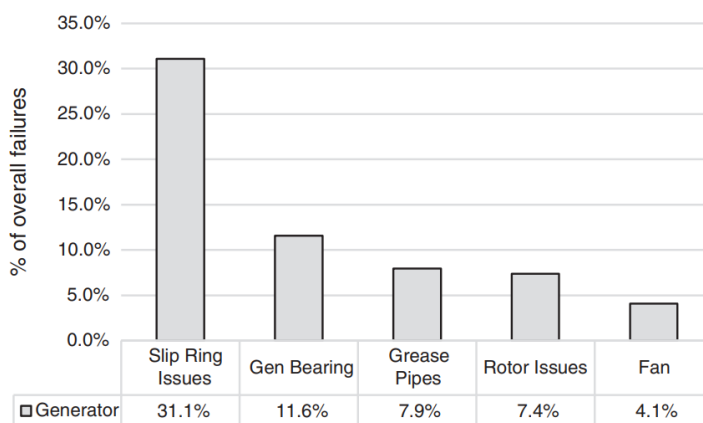|	Slip Ring Issues	Gen Bearing	Grease Pipes	Rotor Issues	Fan
▯ Generator	31.1%	11.6%	7.9%	7.4%	4.1%

Figure 3 Generator Failure modes

An alternative to slip ring-based power transfer is the wireless power transfer using inductive or capacitive devices. These devices are called wireless slip rings, or simply wireless power transfer systems. The characteristics of inductive power transfer technology power level capabilities and factors affecting efficiency is discussed next.

1.2 Inductive power transfer

The design of the inductive power transfer system is based on Ampere's law of Faraday's law of induction which states that a changing current through the coil will produce a time-varying field, which is "absorbed" by the receiving coil, leading to a changing current induced in the coil. If the circuit of the secondary side is closed, Faraday's law is met. As shown in Figure 4, electrical energy is transferred between the coils through the magnetic field. The transmitter and receiver coils together form a transformer. An oscillating magnetic field is formed by giving alternating current to the transmitting end, and then through Ampere's law, Faraday's law of induction passes the magnetic field through the coil and induces an alternating electromotive force to form alternating current at the receiving end. The oscillator will promote the generation of higher frequency alternating current, which greatly improves the transmission efficiency.
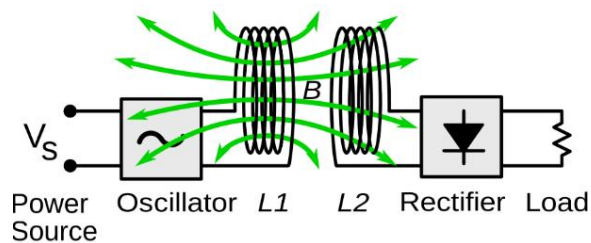

Figure 4. Generic block diagram of an inductive wireless power system

The working frequency of inductive coupling is generally kHz, and the distance between two coils is usually a few millimetres to a few centimetres. As the distance increases, the power efficiency decreases. However, in the case of short distances, the power efficiency can be very high. The performance of this system, namely power transfer efficiency (PTE), is determined by the coupling coefficient and the quality factor k which represents the coupling coefficient between transmitter and receiver and it is a ratio that varies from 0 to 1. Q is the unloaded quality factor of the transmitter's or receiver's coil. Q can be calculated from the coil inductance as in (1), where ω is the angular frequency, L is the coil inductance, and R the loss resistance of the coil. The formula of k, Q and PTE are shown below [6]:

$$Q = \frac{\omega L}{R} \tag{1}$$

$$PTE = \frac{k^2 Q_t Q_r}{[1 + \sqrt{1 + k^2 Q_t Q_r}]^2} \tag{2}$$

Magnetically coupled resonant wireless power transmission (MCR-WPT) is an improvement based on inductive coupling that is used to extend the separation between transmitting and receiving coils while retaining high efficiency power transfer. MCR-WPT generates and transfers energy between two resonant coils through an oscillating magnetic field, which can be achieved with high energy transmission efficiency and small external non-resonant leakage [7]. The MCR-WPT system consists of several parts, including a high-frequency AC power supply, the resonance coil, the rectifying filter circuit, and the compensation network structure of the receiving and transmitting end (more information on compensation networks can be found in section 2.3). When the coil works at the same resonance frequency, power transfer efficiency reaches a maximum value so that maximal power can be transmitted to the load.

1.2.1   High Power, Inductive Wireless Power Transfer technologies in industry.

The field of high-power wireless power transfer has found a niche of application in the transport industry, with systems used for buses, automobiles, and trains, where the development has focused on improving the efficiency for large air gap conditions. Furthermore, research is actively ongoing to develop high-power high efficiency and large air gap wireless power transfer systems for commercial and military applications. Table 1**Error! Reference source not found.** shows a survey of some recent high-power wireless power systems. As seen in the table, in general the efficiency of the wireless power system is linked to the length of the air-gap. However, by changing the oscillating frequency of the transmitting coils and using additional compensation networks, high efficiency can be obtained for larger air-gap systems.

INSTITUTE/ COMPANY	POWER TRANSFER	AIR-GAP (mm)	EFFICIENCY	FREQ. (kHz)	TYPE
KAIST [8-10]	27kW	200	74%	20	Track
	22kW	200	71%	20	Track
WAVE [11]	50kW	178	92%	23.4	Coil
ETH Zurich [12-15]	50kW	100- 200	95.8%	85	Coil
Fraunhofer [16, 17]	22kW	135	97%	100	Coil
KRRI [18]	818kW	50	82.7%	60	Track
Showa Aircraft Co [19]	30kW	150	92%	22	Coil
NYU [20, 21]	25kW	210	91%	85	Coil
Conductix Wampfler [15]	120kW	40	90%	20	Coil

Table 1: Recent high-power wireless power transfer systems

Inductive wireless power transfer systems are also referred to as transformers with air-gaps or rotary transformers when there exists an angular motion between receiving and transmitting coils. In the rotary transformer configuration, the efficiency and performance is the same as a static wireless power system if the coils remain aligned to each other.

In the specific case of the XROTOR, the advantages of having a large circumference to deploy windings and the capacity of selecting small air-gaps between rotating windings, can be exploited to enable MW level wireless power transfer at high efficiency. The design of a rotary transformer for such capabilities is presented in the next section.

2   Design of a Rotary Transformer for the XROTOR

Rotary transformers (RT) are adopted to transfer energy from primary to secondary in situations in which the two sides are in relative rotation. These devices are cylindrical transformers with two cores and the corresponding winding separated by an air gap.

2.1   Basic principles

The structure of an Induction-Based Rotary Transformer is shown in Figure 5a. Its cross section is shown in Figure 5b, and its working theory is like that of a transformer with an air gap. When injecting AC current into the primary windings, a magnetic field will be created in the iron core and induced voltage in the secondary side. With the air gap, there could be relative movements between both sides. In this way, energy could be transferred from the stationary side to the rotary side [22].
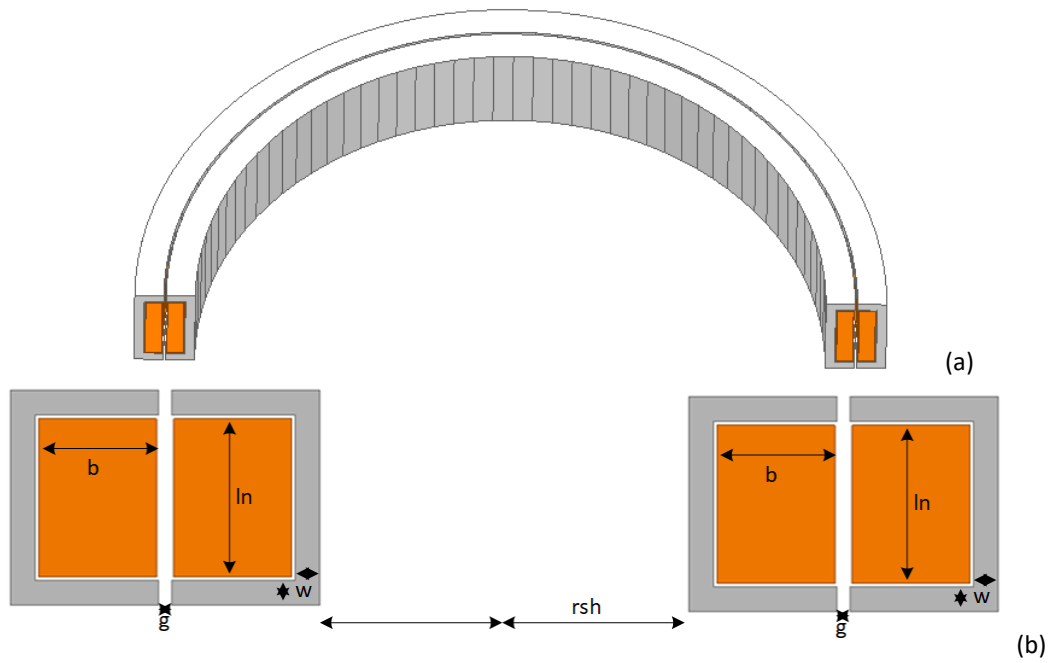
Figure 5: radial-flux RT structure

The system model of RT can be divided into a circuit model and a magnetic model. The circuit model is represented by the self-inductance and mutual-inductance, as shown in Figure 6, where L_{l1} and L_{l2} represent the leakage-inductance of primary and secondary coils, respectively, R_1 and R_2 represent the resistance of both coils, respectively, and M is the coil's mutual inductance value on both sides [23].
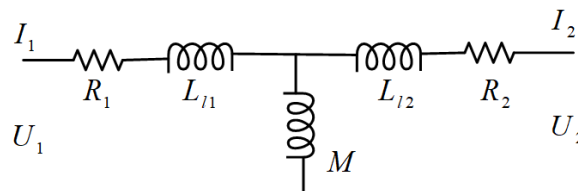

Figure 6: electrical model

The magnetic model is represented by the magnetic equivalent circuit that includes the reluctances and magnetomotive forces as shown in Figure 7. The geometrical parameters are also shown in Figure 5b.
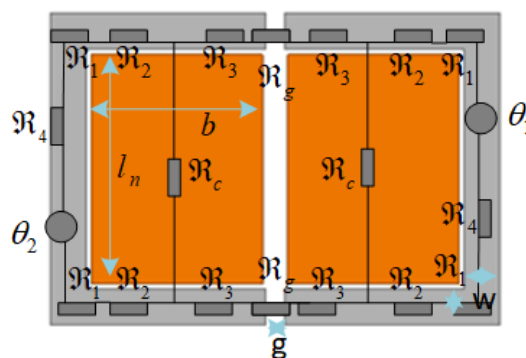

Figure 7: magnetic equivalent circuit

2.2 Design procedure

To start the design, first a simplified magnetic equivalent circuit is considered as shown in Figure 8. To produce a specific magnetic flux density of B_g in the air-gap, the following relationship between the air-gap length (g), air permeability (μ_0) and number of turns (N) is obtained:
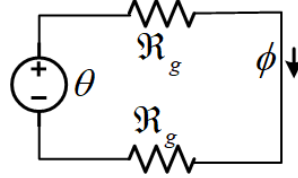
$$NI = \frac{2gB_g}{\mu_0} \tag{3}$$

Figure 8: simplified magnetic equivalent circuit

In Figure 8, $\mathfrak{R}_g$ is the air-gap reluctance, ϕ is the air-gap flux, and θ is the magneto motive force of one coil. Faraday's Law relates the impressed voltage (v) on a winding to the rate of change of flux density (B) as:

$$v = -NA_c \frac{dB}{dt} \tag{4}$$

where A_c is the effective cross-sectional area of the magnetic core. Then induced rms voltage is:

$$V_{rms} = KfNBA_c \tag{5}$$

For a sinusoidal waveform $K = 4.44$ and for a square waveform $K = 4$ and f is the frequency.

The above equation applies to each winding of the transformer. Taking the sum of the volts–amp (VA) products for each winding of the transformer gives [24]:

$$\sum VA = KfBA_cA_wJk_{cu}k_c \tag{6}$$

where k_{cu}, k_c are the winding fill factor and lamination fill factor, respectively. A_w is the winding cross sectional area and J is the current density.

The above sizing equations help us to calculate the main geometrical parameters such as winding and core cross sectional areas, core thickness, and number of turns based on the initial parameters and the required output parameters of the RT.

Having the geometrical and electromagnetic parameters, we can calculate the electrical model parameters of the RT.

To calculate the self-inductances (L_{11}, L_{22}), the equivalent reluctance ($\mathfrak{R}_{eq.}$) seen by each magneto motive force is required. Then:

$$L_{11} = L_{22} = \frac{N_1{}^2}{\mathfrak{R}_{eq.}} \tag{7}$$

To calculate the mutual inductance (M), the flux produced (ϕ'') by each magnetomotive force and passes through the other magnetomotive force should be calculated from Figure 7. So,

$$M = N_1N_2 \frac{\phi''}{\theta} \tag{8}$$

Based on the geometry of the winding, inner and outer winding resistances are calculated by (11).

$$R_{in} = \frac{\rho_{cu}}{a_{cu}} N \times (2\pi(r_{sh} + w + b/2))$$

$$R_{out} = \frac{\rho_{cu}}{a_{cu}} N \times (2\pi(r_{sh} + w + g + 3b/2)) \tag{10}$$

where, a_{cu} is the wire cross sectional area and ρ_{cu} is the copper resistivity. But the effect of high frequency on the AC resistance should be considered from the viewpoint of skin and proximity effects, this is:

$$k_s = \frac{R_{ac}}{R_{dc}} \tag{12}$$

where k_s depends on the conductor radius and the skin depth.

Finally, using the Steimetz equation, the core loss can be estimated by:

$$P_{fe} = k_c . f^\alpha B_m{}^\beta . W \tag{14}$$

where B_m is the peak flux density, W is the weight of cores, and k_c, α and β are the Steimetz coefficients. The preliminary parameters of the RT are reported in Table 2. It should be noted that from the XROTOR tower's dimensions: outer radius of the inner cylinder (shaft) is 1220mm, and inner radius of the outer cylinder is 5470mm. Accordingly, the shaft radius of RT and maximum permissible outer radius of it has been selected based on that.

Parameter	Value	Parameter	Value
rms voltage (V)	850	rsh (mm)	650.00
frequency (Hz)	2000	g (mm)	5.00
flux density (T)	0.50	ρ_{cu} (copper resistivity)	1.72E-08
Power (VA)	333 KVA	μ_r (relative permeability)	300
winding fill factor	0.30	lamination fill factor	0.85
current density (A/mm^2)	2.00	fringing effect factor	1.10

Table 2: preliminary parameters

In high frequency high power applications, there are four main parameters that should be taken into consideration; specific core loss or core loss density, saturation flux density, relative permeability, and temperature characteristics [25]. Among all soft magnetic materials, nanocrystalline and ferrite have higher priority for high frequency high power applications due to low core losses, however using ferrite material, one should compromise with the larger core cross sections, due to lower saturation level.

Considering (**3**) to (**14**) and the preliminary parameters of Table 2 , the parameters of the designed RT are as shown in Table 3.

Parameter	Value	Parameter	Value
rms current (A)	392	b (mm)	40
conductor cross sec. (mm^2)	196	N	10
A_w (mm^2)	6635	$R_{in,ac}$ (ohm)	0.0113
A_c (mm^2)	22162	$R_{in,ac}$ (ohm)	0.0120
w (mm)	20	$R_{out,ac}$ (mH)	2.43
l_n (mm)	166	M (mH)	0.06

Table 3: designed RT parameters

2.3 Compensation Strategy

Compensation circuits are often introduced in an inductive power transfer system to improve the input-power-factor and to increase load power by cancelling out reactive powers generated from loosely coupled coils.

The compensation schemes of an inductively coupled coil set can be classified by the number of compensation capacitors and inductors, the configuration of compensation circuits, and the type of sources. There exist four basic compensation topologies that are widely used. These are Series-Series (SS) topology, Series-Parallel (SP) topology, Parallel-Series (PS) topology and Parallel-Parallel (PP) topology [26].

To increase the power transfer capability of an inductive power transfer system in all the topologies, it is necessary that the system operates at the secondary resonance frequency. When operating at this frequency (ω_0), the impedance of the secondary as seen by the primary is purely resistive in nature, such frequency is defined as:

$$\omega_0 = \frac{1}{\sqrt{L_{22}C_2}} \tag{16}$$

where C_2 is the secondary circuit capacitance. By appropriate selections of the source angular frequency and two compensation capacitances, the operational characteristics (efficiency, power transfer, output voltage or current, etc) of the inductive power transfer systems can be improved.

At near zero phase angles between the primary input voltage and current condition, the voltage and current ratings of the power supply are minimized which in turn implies reduction in cost. There is theoretically no limit to the power transfer capability of a given electromagnetic coupling structure and compensation topology if the system is operated at the secondary resonant frequency.

Here, the primary compensation capacitance is deliberately designed to make the operational frequency (primary zero phase angle frequency) equal the secondary resonant frequency and as such in theory can meet any power transfer requirement without physical changes to the coupling structure and compensation topology. The required primary compensation capacitance is found to be independent of the load if the primary is series compensated. When the primary is parallel compensated, the required primary compensation capacitance is a function of the load. In this case, the primary compensation capacitance must be designed for the required power since it is impractical to allow the primary compensation capacitance to vary with the load.

SS and SP topologies are used and analysed in different inductive power transfer systems. If the primary voltage is maintained constant, then the load current remains constant and hence the SS topology acts as a constant current source. In SP topology, the output voltage is independent of the load and will be constant if primary voltage is maintained constant. In other words, SP topology will behave as a constant voltage source if the voltage across primary is maintained constant.

It should be noted that for a parallel-compensated primary, the capacitance is dependent on the load resistance.

The inductive power transfer system of the RT was simulated in MATLAB for different load conditions. SP compensation topology for this RT considered to improve the active power transfer capability where the capacitance of primary and secondary was calculated to be 53 μF and 2.5 μF, respectively. The effect of load on electrical variables is shown in Figure 9.

2.4 Numerical Simulations

Figure 10 shows one-half of a simulated 3D structure of the RT while the inner parts are moved to a higher level for better presentation.

Topology	Capacitance (F)	Circuit
SS	$$\frac{1}{\omega_0{}^2 L_p}$$	SERIES TO SERIES TOPOLOGY
SP	$$\frac{1}{\omega_0{}^2 (L_p - M^2/L_s)}$$	SERIES TO PARALLEL TOPOLOGY
PP	$$\frac{L_p - M^2/L_s}{\left(\dfrac{M^2 R_L}{L_s{}^2}\right)^2 + \omega_0{}^2 \left(L_p - M^2/L_s\right)^2}$$	PARALLEL TO PARALLEL TOPOLOGY
PS	$$\frac{L_1}{\left(\dfrac{M^2 \omega_0{}^2}{R_L}\right)^2 + \omega_0{}^2 L_p{}^2}$$	PARALLEL TO SERIES TOPOLOGY

Table 4: Primary capacitor topologies [27]
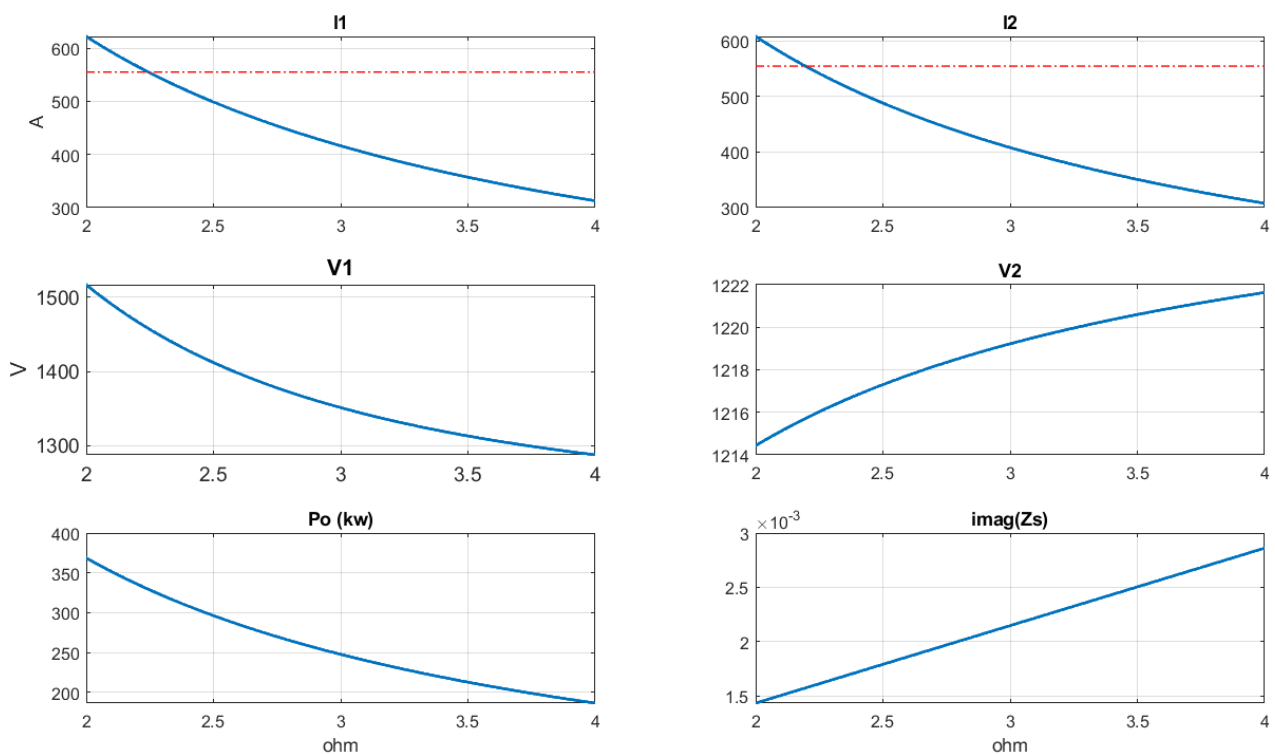
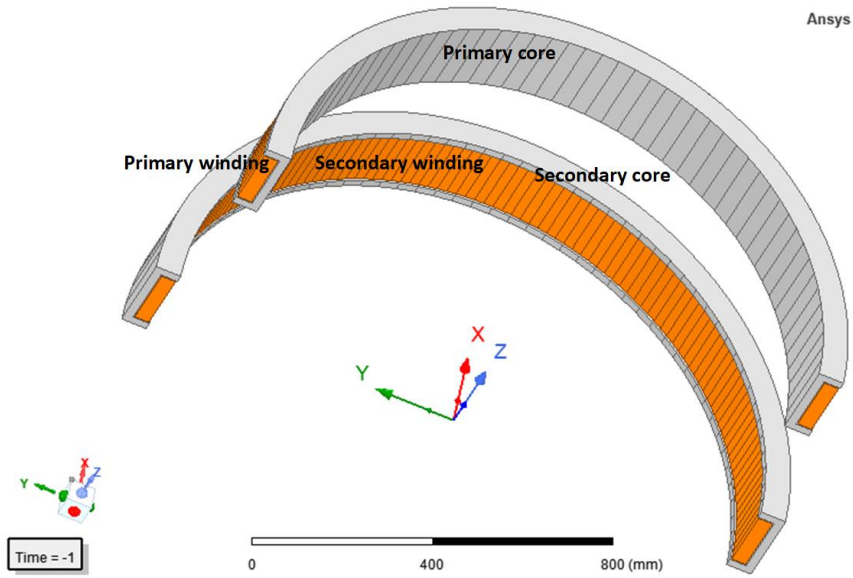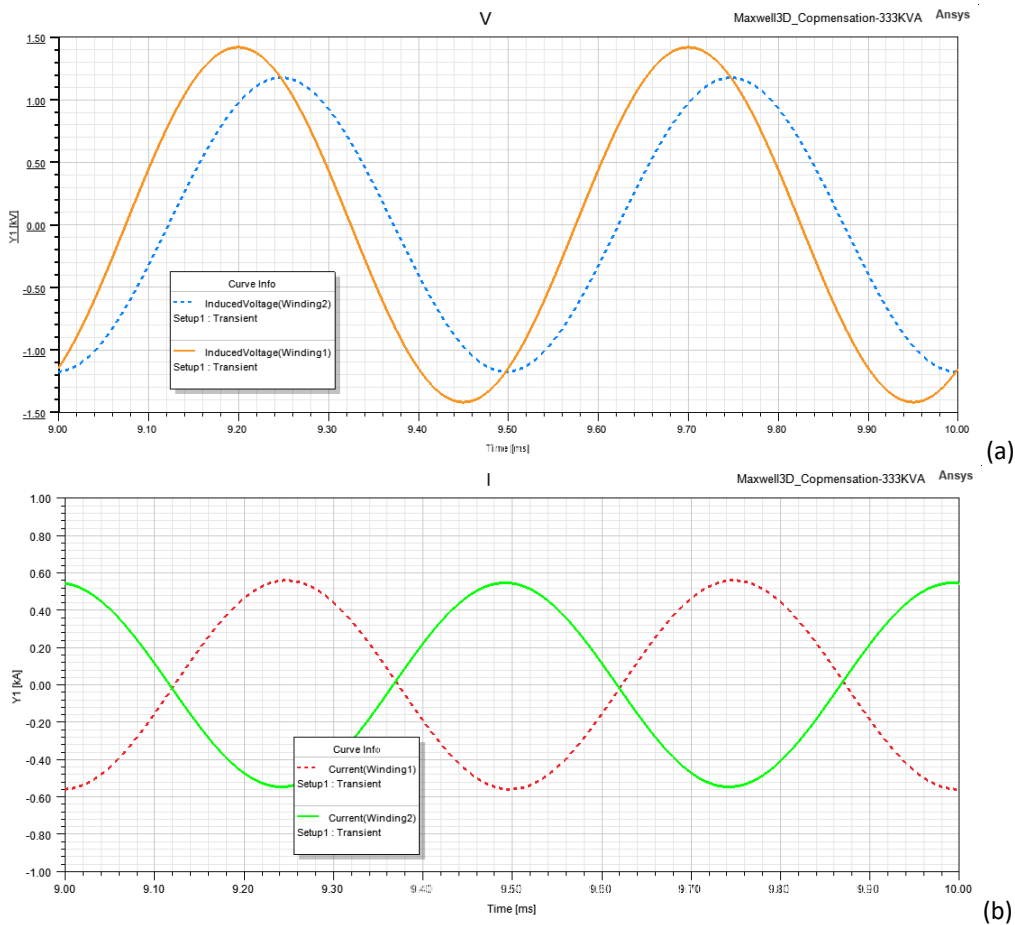**Figure 9: electrical variables vs load resistance**

Figure 10: 3D structure of the RT

To show the electromagnetic performance of the designed RT, 3D simulation, using Finite Element Analysis (FEA) was performed with the results of Figure 11 and Figure 12.
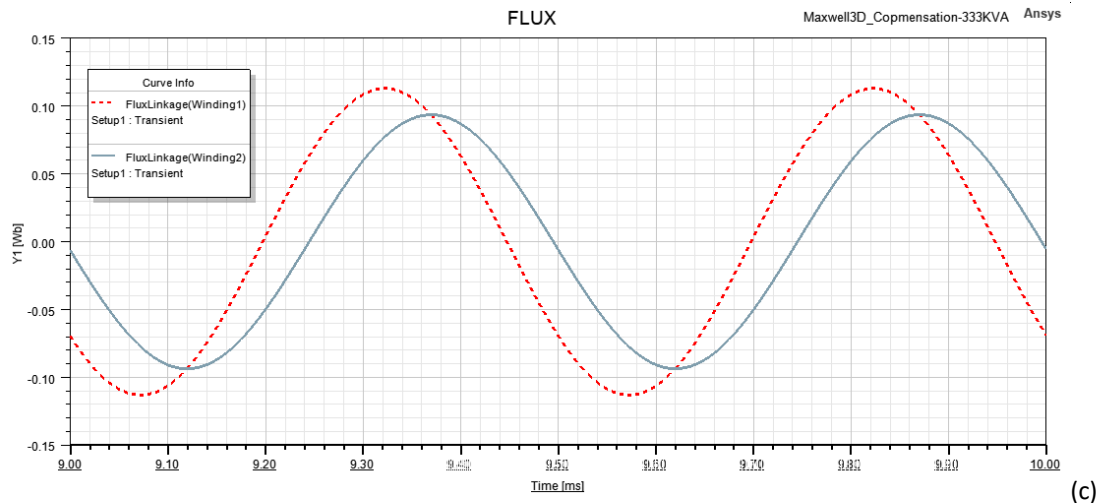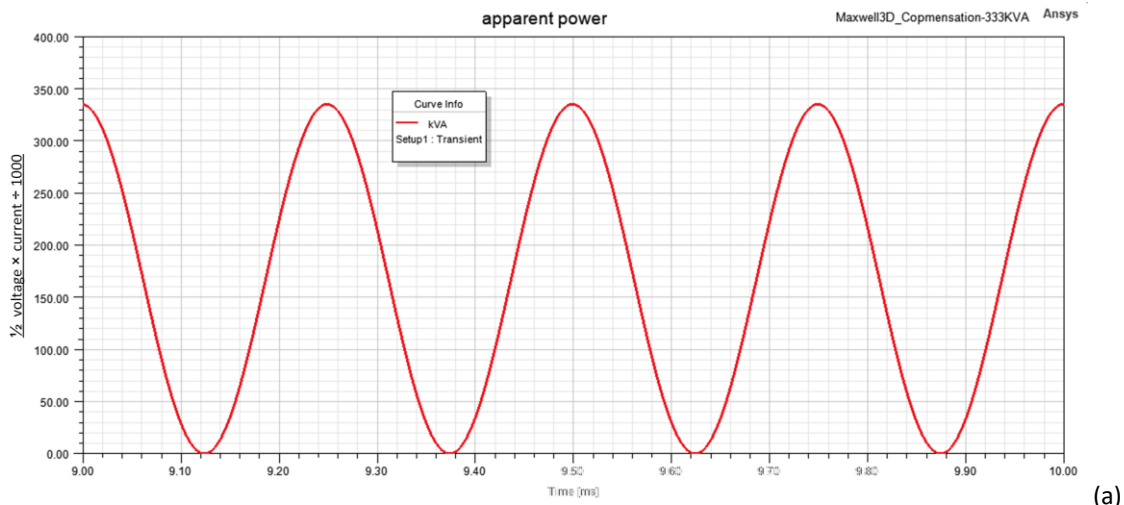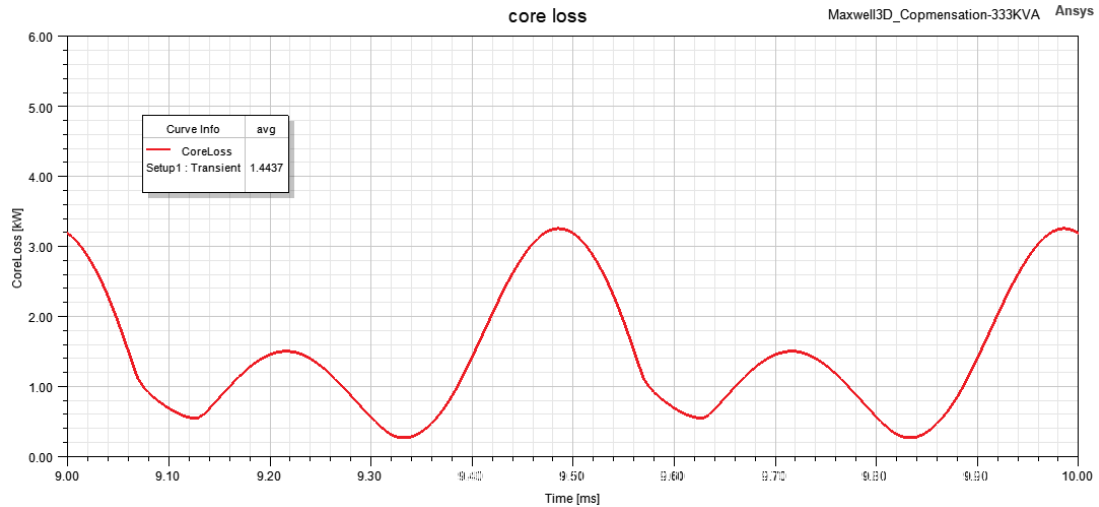

(a)

(b)

(c)

Figure 11: 3D FEA, a) voltage, b) current, c) flux


(a)

(b)

(c)

Figure 12: 3D FEA, a) apparent power, b) output power, c) core loss

As seen in Figure 11 the voltages, currents, and fluxes are sinusoidal, which confirms that there is no saturation in the core, as well as the proper simulation time step. Moreover, Figure 12 shows that the designed RT works at nominal VA, and the compensation strategy is able to improve the power factor and power transfer capability.

For the result of Figure 12.c, the loss versus flux density curve of the core material was implemented in Ansys Maxwell® which calculates the core loss based on the flux density of different parts of the core, as well as the material mass density and its lamination thickness. It is worth mentioning that to eliminate the eddy current loss, laminated cores are considered for both primary and secondary.

Results of Figure 11 and Figure 12 are in good accordance with the electrical circuit solution and as a result, the electrical circuit model could be used in its place when integrating the designed RT with power electronics converters.

To show the effectiveness of the compensation strategy, the input voltage and current of the RT in two conditions (uncompensated, compensated) are compared in Figure 13. As shown in Figure 13 b) for compensated RT, the input voltage and current are almost in phase, which implies much higher efficiency and much less effect of leakage inductances.
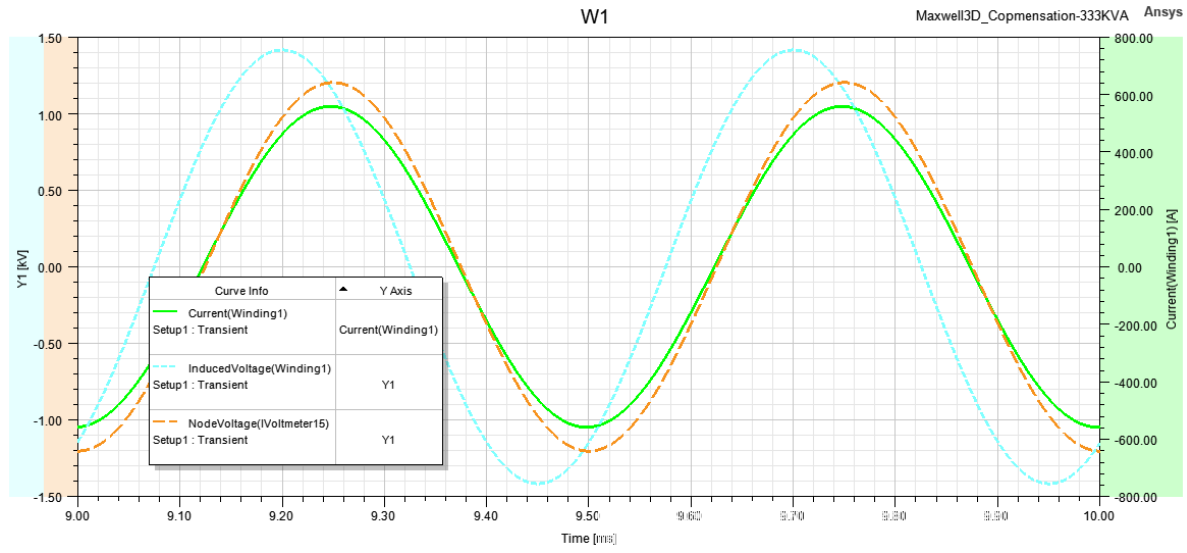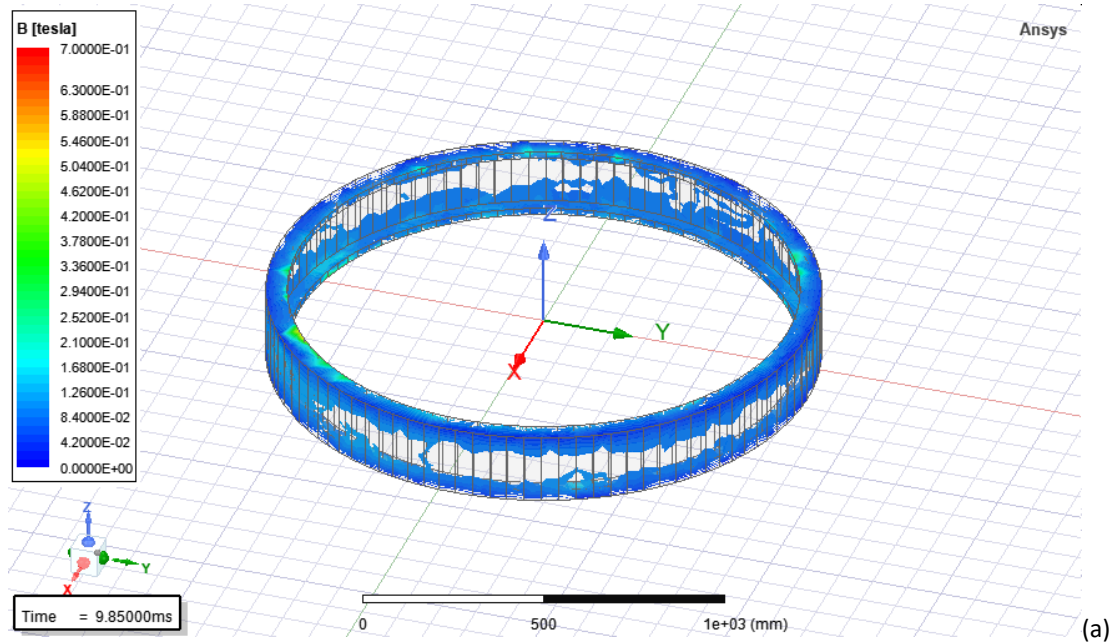

(a)

(b)
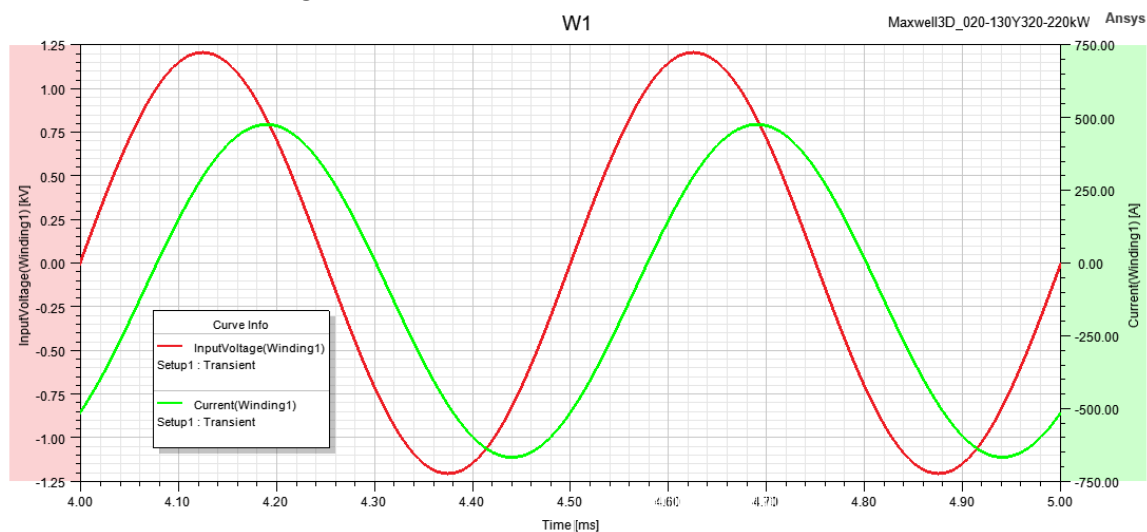
Figure 13: effect of compensation, a) uncompensated, b) compensated

Figure 14 shows the magnetic flux density in various parts of the RT to ensure no saturation occurs. The FEA simulation result shows a few points with high flux density in the structure that are because of sharpness in the edges, but does not affect the overall performance of the system.

(a)

The losses of the RT for above finite element simulation are reported in Table 5.

output power	core loss	copper loss
315.7 kW	1.44 kW	3.45 kW
Efficiency		98.5%

Table 5: losses and efficiency

The core loss could be represented in the electrical circuit of the RT by a parallel resistance ($\cong$500 ohm) to the magnetising inductance.
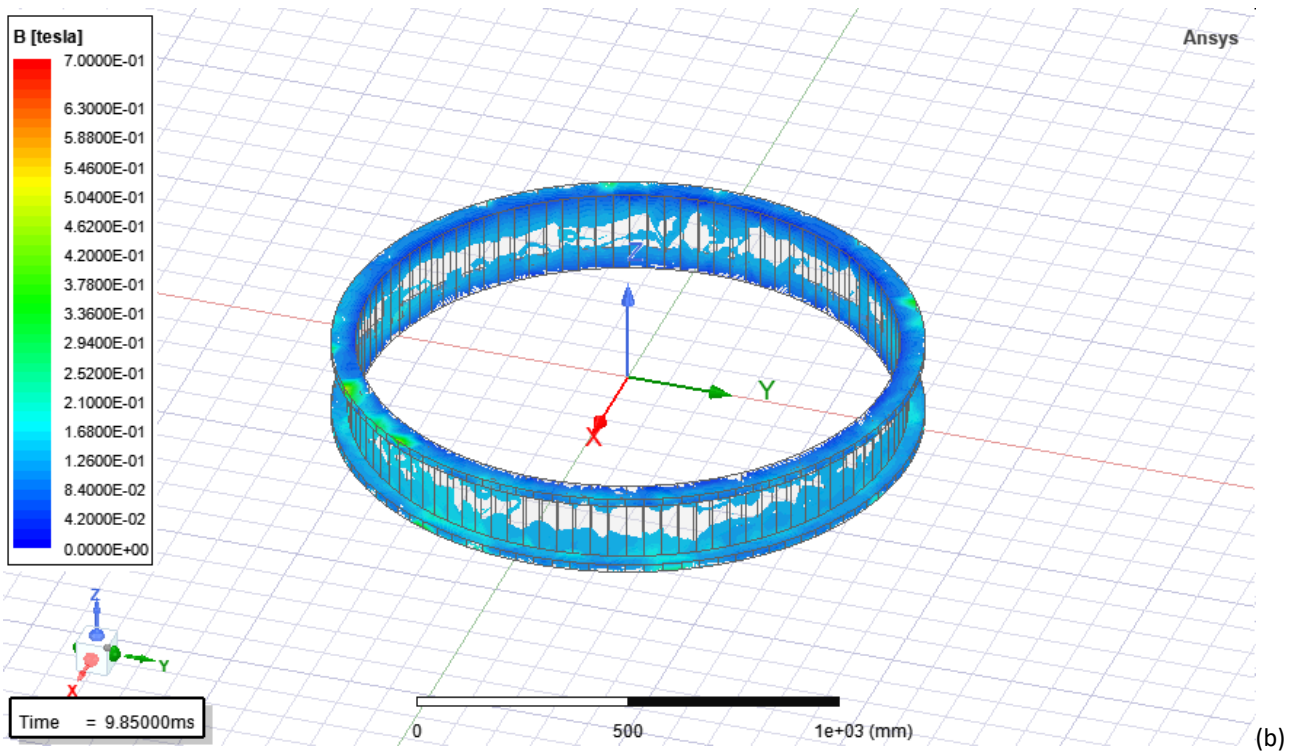
Figure 14: magnetic flux density: a) primary, and b) secondary

2.5 Engineering Considerations for the design of the RT system

2.5.1 Core material

The most important part of manufacturing the RT is the core material selection. Core loss has a considerable influence on the efficiency of the RT. Ideally, low power dissipation, high polarization and mechanical strength are required for the core selection.

Here, electrical steel for e-mobility and high frequency applications is suggested. This electrical steel has low loss and high frequency capability as shown in Figure 15.
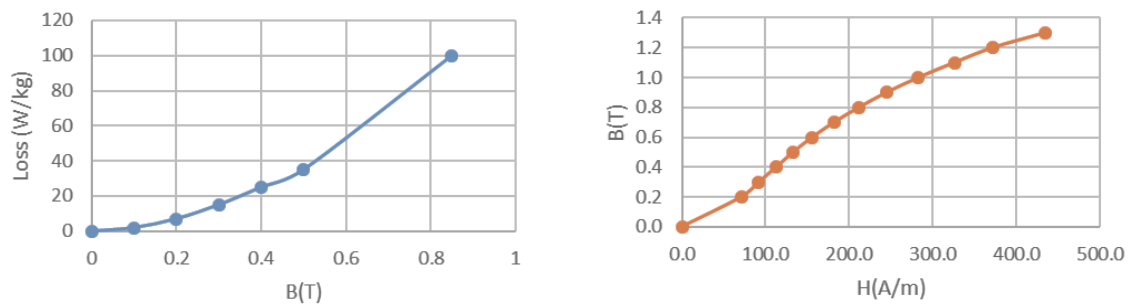

Figure 15: core material characteristics at 2000 Hz

To evaluate the performance, "powercore® 020-130Y320" was selected and its electromagnetic characteristics (B-H curve, core loss curve) were used in the numerical simulation. Nonlinear magnetic characteristic of the core results in slight differences in the output characteristics of the RT nevertheless.

2.5.2   Air-gap

For the designed RT, the air-gap is assumed to be 5 mm. This is reasonable as the rotational speed is low enough and the axial length of the RT is small enough (about 200 mm) to be held constant by proper bearings. Nevertheless, the design could be modified based on the mechanical considerations.

If due to the manufacturing tolerance limitations a larger air-gap is not avoidable, lower power factor due to higher values of the inductances could be improved by suitable compensation strategies. If the compensation strategy is unable to improve the power transfer capability considerably, perhaps higher ratings of the RT should be designed to reach the desired active power transfer performance.

Theoretically, the maximum air-gap is not constrained, but regarding the electromagnetic design and performance of the system, for this RT, the maximum value of a centimetre is recommended.

2.5.3   Wire cross-section area

The cross-sectional area of the wire was calculated to be 196 mm^2 which is not a standard wire gauge. However, the low winding fill factor selected in this design allows the use of multiple wires to make the required wire cross section for the winding.

2.5.4   Thermal analysis

To verify the winding over temperature, first the total outer area for heat transfer is calculated (A_f). Then adding an equivalent heat transfer coefficient (α_t), the winding over temperature is:

$$T_w = \frac{coreloss + copperloss}{\alpha_t . A_f} \tag{17}$$

For this case study, assuming a heat transfer coefficient equal to 20 (W/m^2 °C), results in 82°C increase in the winding. If a lower temperature is preferred, some ventilation should be considered for the RT system.

Based on the FEA, a heat transfer analysis and temperature distribution was also done with a package of Ansys Electronics Desktop. For that, the ambient temperature and the equivalent heat transfer coefficient are assumed to be 40 °C and 30 W/m^2 °C, respectively.

Figure 16 shows the temperature distribution in both windings and Figure 17 shows it in both cores. As it can be seen, windings are more subject to over temperature and perhaps some additional cooling systems are required.

It should be noted that results are reasonable as the frame area of the RT is such that heat dissipation from the surface is low. Nevertheless, due to its low losses, it does not require complicated and expensive cooling systems.
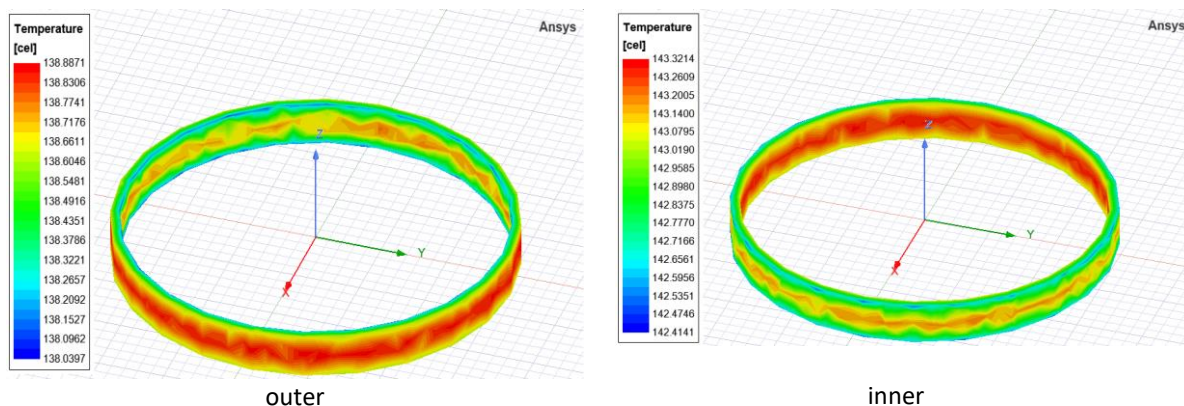

outer   inner

Figure 16: temperature distribution in windings

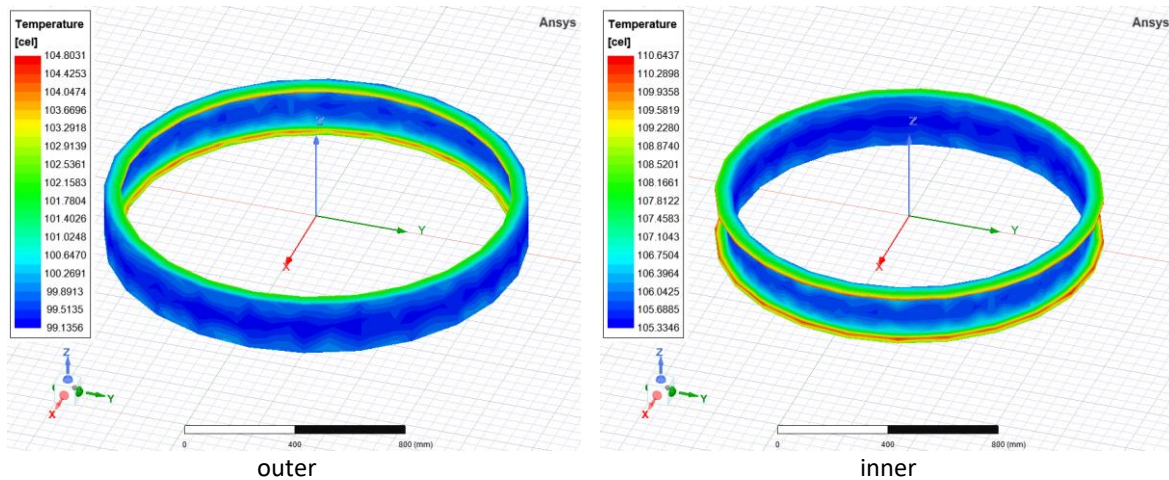<div align="center">outer   inner</div>

Figure 17: temperature distribution in cores

3   Dual active bridge converter

3.1 Introduction

The bidirectional Dual-Active-Bridge (DAB) is a power electronic structure used to interface high frequency transformer systems for energy conversion and it is used extensively in wireless power transfer system applications working at KHz-Frequency levels, (such as the RT windings). The DAB converter has become an attractive solution in electric vehicle, hybrid electric vehicle and high power-density aerospace applications because of its bidirectional power flow, galvanic isolation, high efficiency, and Zero-Voltage Switching (ZVS) [28], [29].

The three-phase DAB converter is generally considered in bi-directional applications since it has the advantages of the single-phase DAB converter such as soft switching capability without additional resonant components and smooth bidirectional power transition using a simple control structure. In addition, the 3P-DAB converter shows low conduction loss and high-power density because of its interleaved structure. The interleaved structure makes the "effective" switching frequency to increase, which can decrease the size of passive components and reduce the peak and root mean square (RMS) current [30]. Compared to single-phase DAB converter, three-phase DAB converter has higher power capability and lower ripple current on both the input and output side, which leads to lower capacitor volume and thus higher power density [28].

Unlike the single-phase counterpart, the three-phase structure can triple the effective frequency and reduce the amplitude of the ripple. Hence, input and output filters can be downsized; the transformer RMS current is also lower and power density is higher than that of the single-phase version [31].

It should be noted that when the voltage ratio between the primary and secondary sides mismatches the transformer turn ratio, hard switching may occur and lead to excessive switching loss, especially at partial load.

For single-phase DAB converters, advanced modulation strategies have been proposed to overcome the drawback of phase shift modulation, including extended-phase-shift, dual-phase-shift and phase-shift plus pulse-width modulation. These advanced modulations require phase shift between the two half bridges in the same H-bridge, and thus the duty cycle of the AC voltage applied to the transformer can be controlled lower than 50%. In three-phase DAB converter, however, each phase has one half bridge, and the phase shift

between three phases are fixed at 120°, which makes the advanced modulation strategies not applicable [28].

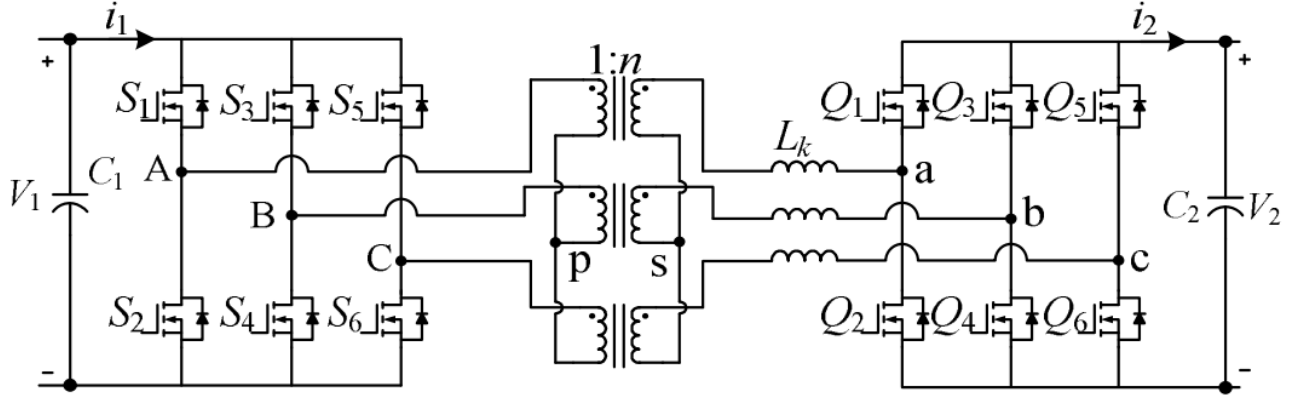The schematic of a three-phase DAB DC/DC converter is shown in Figure 18 [28].

Figure 18. Circuit schematics of three-phase dual active bridge converter interfaced with the RT windings

During operation, six-step line-to-neutral voltages are applied on both side of the RT. Due to the phase shift (ϕ) between primary and secondary side, the voltage difference across the inductance enables power transfer. The operating waveform is symmetrical in both directions. When $\phi < \pi/3$, the relationship between the phase shift and transferred power (P) is given as [28]

$$P = \frac{nV_1V_2}{12\pi^2 f L_k} \cdot \phi(4\pi - 3\phi) \tag{18}$$

where, n is the turn ratio of the transformer, $V_1 and V_2$ and V_1 the primary and secondary voltages, f the frequency, and L_k is the inductance. From (**18**), the output power increases with phase shift ϕ. At a desired power P, ϕ can be calculated as (19).

$$\phi = \frac{2\pi}{3}\left(1 - \sqrt{1 - \frac{9f L_k P}{nV_1V_2}}\right) \tag{19}$$

for three-phase DAB converter with Y-Y connection in the transformer, the power can be defined as follows [32].

$$P = \begin{cases} \frac{V_1 V'_2}{\omega L}\left(2\phi - \frac{3\phi}{2\pi}\right) & for\ 0 \leq \phi \leq \frac{\pi}{3} \\ \frac{V_1 V'_2}{\omega L}\left[3\left(\phi - \frac{\phi^2}{\pi}\right) - \frac{\pi}{6}\right] & for\ \frac{\pi}{3} \leq \phi \leq \frac{2\pi}{3} \end{cases} \tag{20}$$

where $\omega = 2\pi f$. The winding ratio n is defined such that the primary-side referred output voltage is given by $V'_2 = nV_2$. The transformer current can be calculated as follows [32]:

$$i_{L_A} = \begin{cases} \frac{(V'_2 - V_1)\pi}{3\omega L} & for\ 0 \leq \phi \leq \frac{\pi}{3} \\ \frac{(3V'_2 - 2V_1)\pi + 6V_1\phi}{6\omega L} & for\ \frac{\pi}{3} \leq \phi \leq \frac{2\pi}{3} \end{cases} \tag{21}$$

When comparing YY (wye to wye) and ΔΔ (delta to delta) connection for three-phase DAB converter, the first one yields small leakage inductance and higher transformer RMS current leading to a smaller number of turns and a greater number of strands, respectively. The ΔΔ connection requires large leakage and lower

transformer RMS current that leads to a greater number of turns and a smaller number of strands, respectively. The same ZVS characteristic is expected from both YY and ΔΔ connection [32]. Among some transformer configurations, the YY topology requires smaller leakage inductance to send a specific amount of power [31]. It is noted here that, delta-type transformer structures can be transformed into star connection by using the following transformation:

$$L_{Ya} = \frac{L_{Db}L_{Dc}}{L_{Da}+L_{Db}+L_{Dc}}$$ (22)

where, L_D is the delta-type transformer inductance and L_Y is the equivalent Y-type transformer inductance.

To design the transformer, at the first step, some preliminary parameters must be determined:

- Maximum output power
- Nominal input and output voltages
- Current density
- Window utilization factor
- Initial switching frequency and flux density

In the specific case of the RT for the XROTOR, these parameters have already been defined in **Table 2** and **Table 3**.

3.2   Three phase DAB converter design

Here, a 1 MW dual active bridge is designed to be used in the XROTOR project. The following parameters are used in the design process as stated in the previous section:

- Rated power: 1 MW
- DC link input voltage: 1800 V
- DC link output voltage: 1800 V

Therefore, the primary and secondary voltage has 1200 V peak value and the voltage ratio is:

$$n = \frac{V_{pri}}{V_{sec}} = \frac{1200}{1200} = 1 \;,\; M = \frac{nV_2}{V_1} = 1$$

Switching frequency: 2 kHz

When $\phi < \pi/3$, the relationship between the phase shift and transferred power is given as:

$$P = \frac{nV_1V_2}{12\pi^2 f L_k}.\phi(4\pi - 3\phi)$$ (23)

Supposing that the maximum power is delivered at the maximum allowed angle ($\phi_{P_{max}} = \frac{\pi}{3}$), the inductor can be sized as follows:

$$L_k = \frac{nV_1V_2}{12\pi^2 f P}\phi(4\pi - 3\phi) \;\rightarrow\; L_k = 60\mu H$$ (24)

$$I_M = \frac{V_1}{18 f_s L_k} = 1.111\,kA$$ (25)

Since the inductor is in series connection with the primary winding of an ideal transformer in the DAB converter design, the summation of the transformer leakage inductance and the inductor should be 60 μH. The transformer RMS current can be calculated as follows:

$$I_{pri,rms} = \frac{I_M \sqrt{3}}{3} \sqrt{5(1-M)^2 + 27\left(2 - \frac{\phi}{\pi}\right)\left(\frac{\phi}{\pi}\right)^2 M} \tag{26}$$

$$I_{pri,rms} = \frac{1111 \times 1.73}{3} \sqrt{5(1-1)^2 + 27\left(2 - \frac{1}{3}\right)\left(\frac{1}{3}\right)^2 \times 1} = 1434.3A \tag{27}$$

The RMS switch current can be calculated as follows:

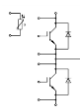$$I_{Qx,rms} = \frac{I_{pri,rms}}{\sqrt{2}} = \frac{1434.3}{1.414} = 1014.2 \ A \tag{28}$$

By considering a 1:1 ratio for the transformer, the same current rating is expected for both side switches.

In order to size the transformer, the American Wire Gauge (AWG) should be considered as shown Table 6 [33]. For frequencies in the range of 1-10 kHz, normally AWG 30 is suggested. It has 0.254 mm diameter and 0.0509 mm^2 cross section area. The maximum current for this single wire is 0.142 A.

Freq. (kHz)	Rec. Wire Guage	Nom. Dia. Over Copper	DC Res. Ohm/m	Single strand R_{ac}/R_{dc}
0.06 to 1	28 AWG	0.0126	66.37	1.0000
1 to 10	30 AWG	0.0100	105.82	1.0000
10 to 20	33 AWG	0.0071	211.70	1.0000
20 to 50	36 AWG	0.0050	431.90	1.0000
50 to 100	38 AWG	0.0040	681.90	1.0000
100 to 200	40 AWG	0.0031	1152.30	1.0000

Table 6 Litz wire sizing based on the frequency

The DC link voltage is 1800 V and the nominal voltage for each switch in the DAB converter would be the same. The rating current should also be more than 1 kA as calculated in previous section. Various solutions are available in the market based on insulated-gate bipolar transistor (IGBT) modules, metal–oxide–semiconductor field-effect transistor (MOSFETs) and bipolar junction transistor (BJTs) as listed in Table 7.

	IGBT
Part number	FF1800R17IP5
Description	IGBT Modules PrimePACK™3+B-series module with Trench/Field stop IGBT5, Emitter Controlled 5 diode and NTC
Specifications	VCES = 1700V IC nom = 1800A / ICRM = 3600A

Price	£1,570.34
Manufacturer	Infineon Technologies
Distributer	Mouser [34]

Table 7. Suggested solution for the power switches.

3.3　DAB converter simulation

A three-phase dual active bridge DC/DC converter is simulated using MATLAB/Simulink, as shown in Figure 20. This circuit consists of two DC voltage source with 1800 V rating. Two three-phase full-bridge converters are connected to each other through inductors and a three-phase transformer with YY connection. To keep the input and output voltages stable, capacitors are considered in parallel with the input and output as shown in Figure 18. The dead-time is considered to be 0.1 microseconds.

To cancel the reactive power required by the RT in the DAB converter, a series connected capacitor is placed in the input of the transformer, as explained in section 2.3. Therefore, capacitors of 140 μF are connected to each phase in series. In addition, capacitors with 100 μF are connected in parallel to the input and output ports to limit DC-link voltage variations to 5%. The RT parameters calculated in Section 2 are used here to integrate the rotary transformer with the DAB converter.

The IGBTs functions like a combined device with a low power MOSFET driving a bipolar transistor. Because the operating current density for bipolar transistors is higher than FETs, an IGBT can carry higher currents than the same size FET. The data sheet of IGBTs provides the voltage drop at specific currents and has the Figure 19 curve that could be used to determine the voltage drop at various currents. An important parameter for the switches in the loss calculation is the on-state resistance, as shown in Figure 19 for a given IGBT.
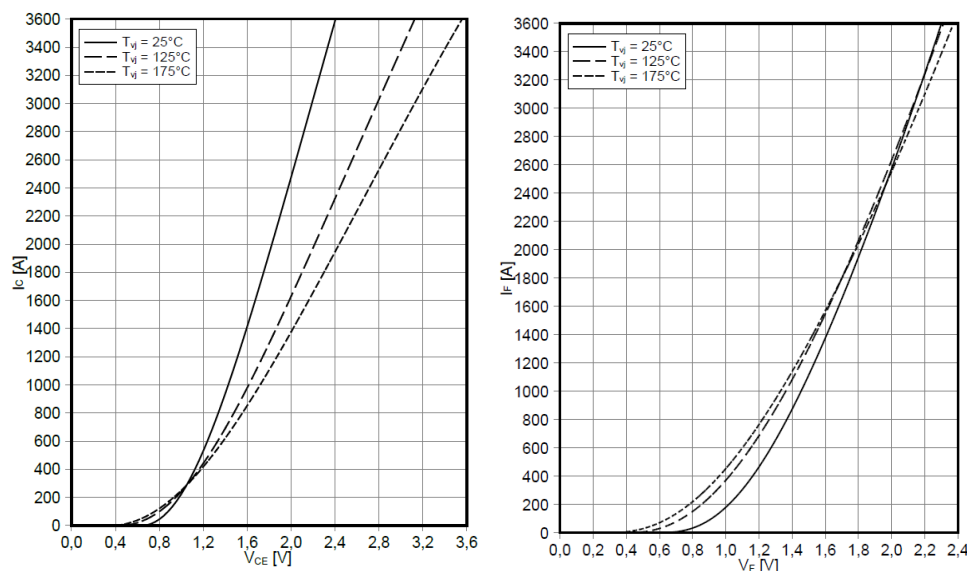

Figure 19. The output characteristic of IGBT FF1800R17IP5 (left) its anti-parallel diode (right).

The on-state resistance for the above switch is calculated and equals 0.375 $m\Omega$. This parameter is included in the simulations. The forward-bias resistance of the diode is calculated in the same way and it is equal to 0.035 $m\Omega$.

The simulation parameters are listed in Annex A: DAB converter parameters.
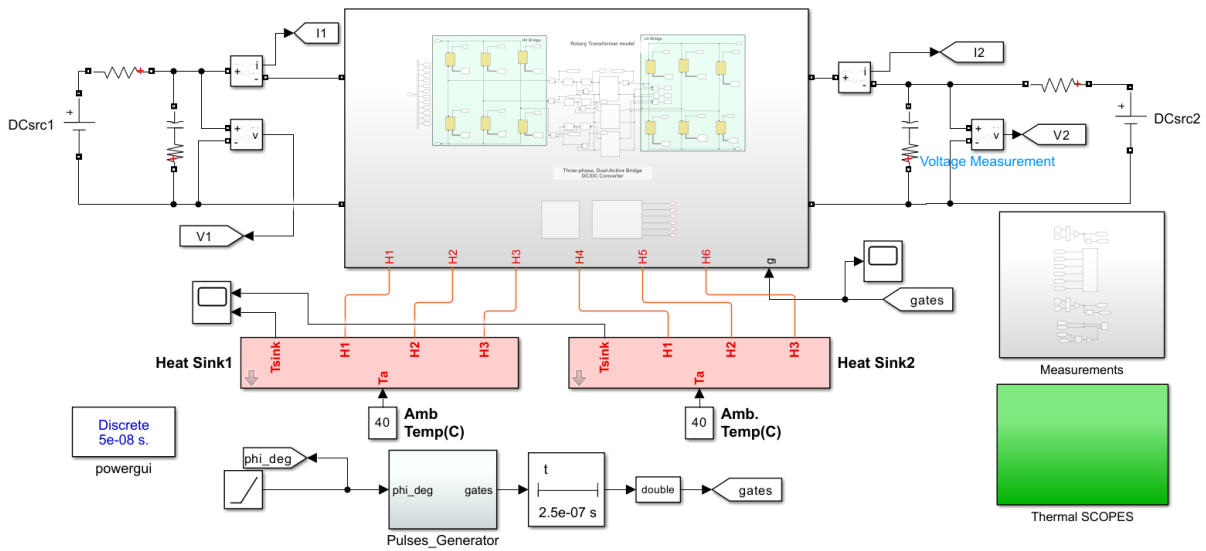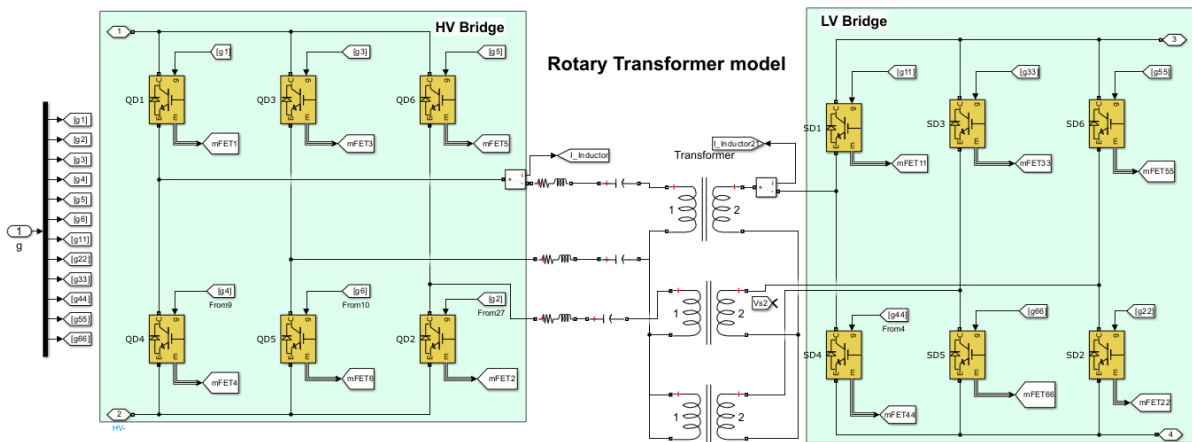

Figure 20. The simulation environment in Simulink

Figure 21. Three-phase DAB converter with rotary transformer simulation in Simulink.
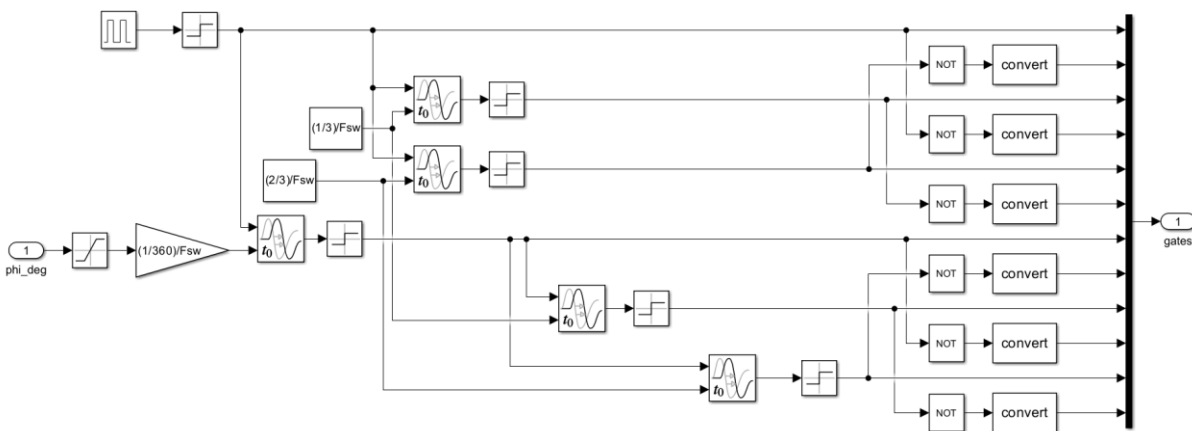

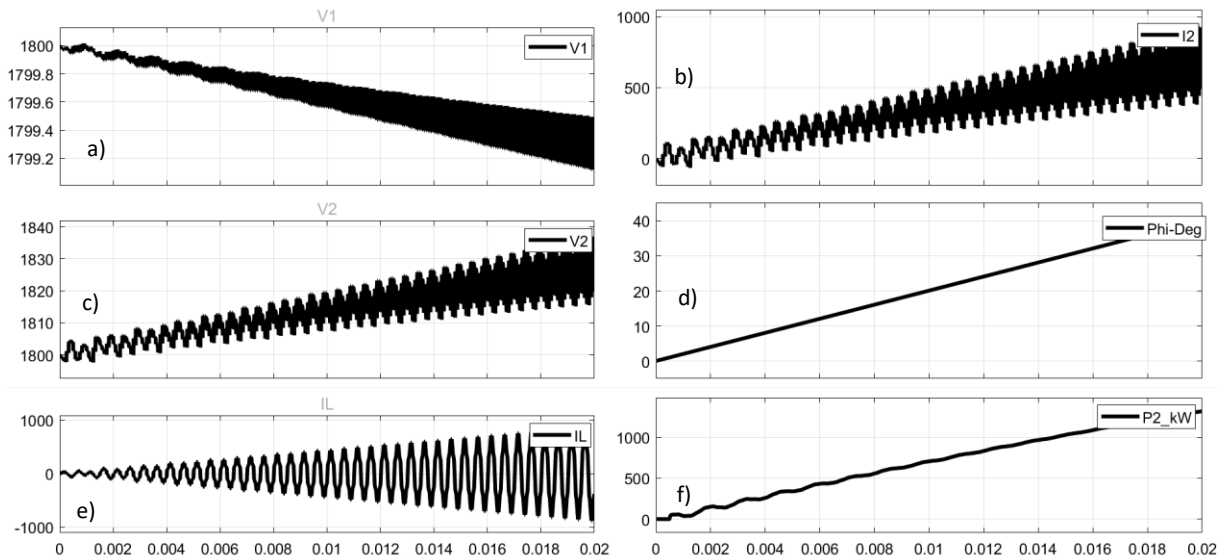**Figure 22. Gate pulse generation for DAB converter switches**

Figure 23. Simulation results for three-phase DAB converter; left: input DC-link voltage, output DC-link voltage, inductor current, right: output current, phase-shift, output power.
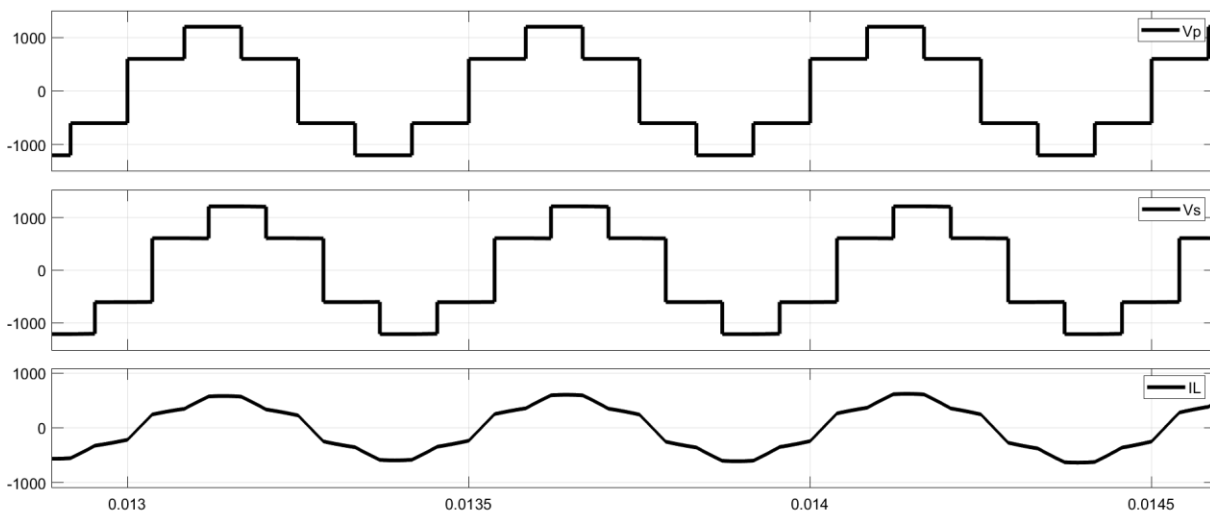

Figure 24. The primary phase voltage, the secondary phase voltage and the inductor current waveforms

In order to simulate the DAB converter, an increasing ramp phase shift is considered here. As shown in Figure 22, the pulse for the upper switch in the first phase of the HV bridge is considered as the reference and the pulses for the other switches are produced based on this signal. Gate pulses should be produced as discussed previously.

The simulation results shown in Figure 23 include the input DC link voltage (V_1), the output DC link voltage (V_2), the inductor current in phase 1 (I_L), the output DC link current (I_2), the phase shift angle (ϕ) in degrees and the output power (P_2) in kW. As seen here, by increasing the phase shift angle (ϕ) from zero to 60 degrees, the output power is increased. The target power output of 1MW is achieved at $\phi = 30°$. The input and output voltages, V_1 and V_2 change between the allowed voltage ranges that are less than 5%.

The rotary transformers primary and secondary voltages and the inductor current with more details are shown in Figure 24.

3.3.1 Three phase DAB losses assessments.

The IGBTs losses are computed as follows:

Turn-on loss: Pre-switching value of the voltage across the device, post-switching value of the current flowing into the device, and the junction temperature are used to determine the energy losses with the help of a 3D lookup table, i.e. $E_{ON} = f(I_C, T)$. This energy is converted into a power pulse which is injected into the thermal network.

Turn-off loss: Pre-switching value of the current flowing into the device, post-switching value of the voltage across the device, and the junction temperature are used to determine the energy losses with the help of a 3D lookup table, i.e. $E_{OFF} = f(I_C, T)$. This energy is converted into a power pulse which is injected into the thermal network.

Conduction loss: Value of the current (I_c) flowing in the device and its junction temperature determine what would be the saturation voltage (V_{ce}) across the IGBT using a 2D look-up table, i.e. $I_C = f(V_{ce}, T)$. This Vce is then multiplied by Ic to obtain the losses which are injected into the thermal network.

The diode's losses are computed as follows:

Reverse recovery loss: Pre-switching value of the current (I_f) flowing into the device, post switching value of the voltage (V_f) across the device, and the junction temperature are used to determine the energy losses with the help of a 3-D lookup table, i.e. $E = f(I_f, V_f, T)$. This energy is converted into a power pulse which is injected into the thermal network.

Conduction loss: Value of the current (I_f) flowing in the device and its junction temperature determine what the on-state voltage (V_f) across the diode would be using a 2D look-up table, i.e. $V_f = f(I_f, T)$. This V_f is then multiplied by I_f to obtain the losses which are injected into the thermal network.

The output of the electrical model, which is the total power loss of the device, is fed into the thermal model. The thermal model uses this value of power loss to calculate the temperature of the components present in the thermal model.

The temperature rise for both input and output side converters has been simulated and the results are shown in Figure 26, respectively. By considering 40°C for the ambient temperature, the heat sink temperature will rise up to 80 °C and 110 °C for the input and output converters, respectively.
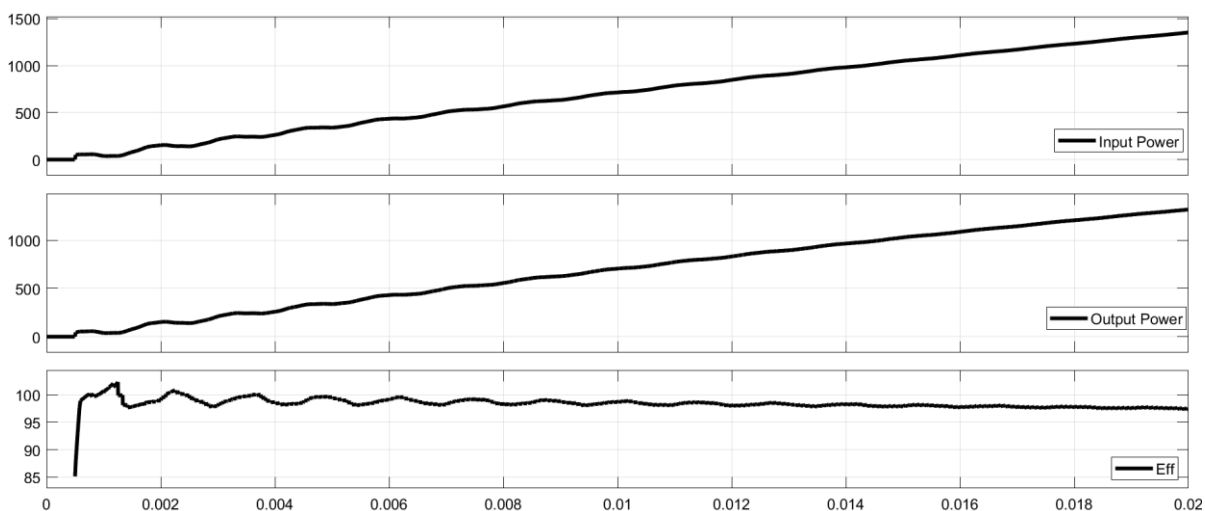

Figure 25. The input power (top), output power (middle) and the efficiency (bottom).
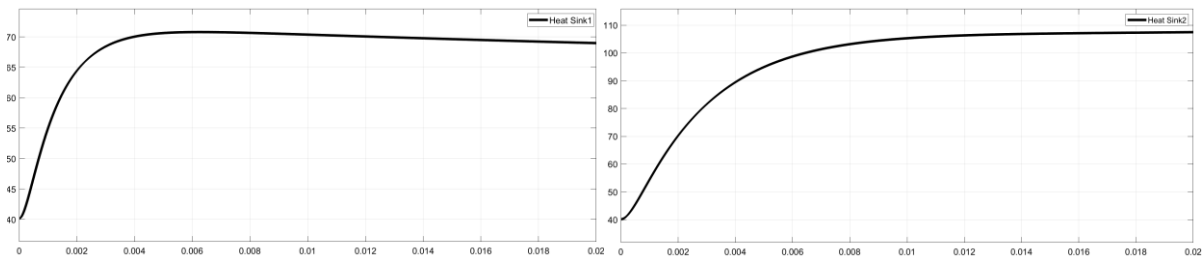
Figure 26. Temperature rise in the heatsink of the input (left) and output (right) converter of the DAB converter.

Another important challenge regarding the use of DAB converters and rotary transformer is the power loss and their efficiency. The input power, output power and the overall efficiency are depicted in Figure 25, respectively. As seen in this figure, the overall efficiency in the nominal power of 1MW is about 98%.

4   Conclusions

This report presented the design and analysis of a RT system to transmit bidirectionally up to 1 MW of power using magnetic wireless power transfer. The design methodology was validated using FEA simulation and all relevant losses (electrical, magnetic, thermal) were quantified to determine efficiency. The engineering considerations to develop the RT system where also revised and compared against current magnetic design practices. In general terms the manufacture of the RT systems is doable with an efficiency of 98.5%.

The second section of this report analysed a power electronic topology capable to drive power bidirectionally through the RT windings. This topology (the DAB) was analysed numerically, electrically, and thermally to quantify performance and efficiency. The simulation results indicate that bidirectional power control can be obtained at the desired switching frequency (2KHz) with overall efficiency of around 98% in the power electronic system.

The results presented in this report indicate that the combined efficiency of the RT and the DAB to enable and control the wireless power transfer in the XROTOR system is 96.53% which the WP5 lead suggests is within the efficiency requirements of the XROTOR project. The XROTOR TMT will review this suggestion.

The design methodology presented in this report can be used to increase the power rating of both the RT and the DAB if necessary, or a parallel deployment of several 1MW systems can be performed to attain a desired power rating. The selection of any these choices can be included in a future cost/redundancy analysis.

5   Bibliography

[1]   C. Flannigan, J. Carroll, and W. Leithead, "Operations expenditure modelling of the XROTOR offshore wind turbine concept," *Journal of Physics: Conference Series,* vol. 2265, no. 3, p. 032054, 2022/05/01 2022, doi: 10.1088/1742-6596/2265/3/032054.

[2]   J. McMorland *et al.*, "A review of operations and maintenance modelling with considerations for novel wind turbine concepts," *Renewable and Sustainable Energy Reviews,* vol. 165, p.

[3]   R. D. Hall and R. P. Roberge, "Carbon brush performance on slip rings," in *Conference Record of 2010 Annual Pulp & Paper Industry Technical Conference*, 21-23 June 2010 2010, pp. 1-6, doi: 10.1109/PAPCON.2010.5556522.

[4]   J. K. SkjØlberg, H. F. Ohma, and M. Runde, "Wear Rates and Current Distribution of Carbon Brushes on Steel Slip Rings," *IEEE Transactions on Energy Conversion,* vol. 24, no. 4, pp. 835-840, 2009, doi: 10.1109/TEC.2009.2025416.

[5]   J. Carroll, A. McDonald, and D. McMillan, "Failure rate, repair time and unscheduled O&M cost analysis of offshore wind turbines," *Wind Energy,* 19, no. 6, pp.

[6]   M. Aboualalaa, H. Elsadek, and R. K. Pokharel, "WPT, Recent Techniques for Improving System Efficiency," in *Wireless Power Transfer–Recent Development, Applications and New Perspectives*: InTechOpen, 2021.

[7]   W. Yan and J. Chen, "A general design of magnetic coupling resonant wireless power transmission circuit," in *IOP Conference Series: Earth and Environmental Science*, 2017, vol. 69, no. 1: IOP Publishing, p. 012197.

[8]   C. C. Mi, G. Buja, S. Y. Choi, and C. T. Rim, "Modern Advances in Wireless Power Transfer Systems for Roadway Powered Electric Vehicles," *IEEE Transactions on Industrial Electronics,* vol. 63, no. 10, pp. 6533-6545, 2016, doi: 10.1109/TIE.2016.2574993.

[9]   S. Y. Choi, S. Y. Jeong, B. W. Gu, G. C. Lim, and C. T. Rim, "Ultraslim S-Type Power Supply Rails for Roadway-Powered Electric Vehicles," *IEEE Transactions on Power Electronics,* vol. 30, no. 11, pp. 6456-6468, 2015, doi: 10.1109/TPEL.2015.2444894.

[10]   S. Y. Choi, B. W. Gu, S. Y. Jeong, and C. T. Rim, "Advances in Wireless Power Transfer Systems for Roadway-Powered Electric Vehicles," *IEEE Journal of Emerging and Selected Topics in Power Electronics,* vol. 3, no. 1, pp. 18-36, 2015, doi: 10.1109/JESTPE.2014.2343674.

[11]   H. H. Wu and M. P. Masquelier, "An overview of a 50kW inductive charging system for electric buses," in *2015 IEEE Transportation Electrification Conference and Expo (ITEC)*, 14-17 June 2015 2015, pp. 1-4, doi: 10.1109/ITEC.2015.7165747.

[12]   R. Bosshard and J. W. Kolar, "All-SiC 9.5 kW/dm3 On-Board Power Electronics for 50 kW/85 kHz Automotive IPT System," *IEEE Journal of Emerging and Selected Topics in Power Electronics,* vol. 5, no. 1, pp. 419-431, 2017, doi: 10.1109/JESTPE.2016.2624285.

[13]   R. Bosshard and J. W. Kolar, "Multi-Objective Optimization of 50 kW/85 kHz IPT System for Public Transport," *IEEE Journal of Emerging and Selected Topics in Power Electronics,* vol. 4, no. 4, pp. 1370-1382, 2016, doi: 10.1109/JESTPE.2016.2598755.

[14]   R. Bosshard, U. Iruretagoyena, and J. W. Kolar, "Comprehensive Evaluation of Rectangular and Double-D Coil Geometry for 50 kW/85 kHz IPT System," *IEEE Journal of Emerging and Selected Topics in Power Electronics,* vol. 4, no. 4, pp. 1406-1415, 2016, doi: 10.1109/JESTPE.2016.2600162.

[15]   R. Bosshard, J. W. Kolar, and W. G. Hurley, *Multi-Objective Optimization of Inductive Power Transfer Systems for EV Charging*. ETH-Zürich, 2015.

[16]   B. Goeldi, J. Tritschler, and S. Reichert, "Measurement Results of a 22 kW Bidirectional Inductive Charger," in *Proceedings of PCIM Europe 2015; International Exhibition and Conference for Power Electronics, Intelligent Motion, Renewable Energy and Energy Management*, 19-20 May 2015 2015, pp. 1-8.

[17]   J. Tritschler, S. Reichert, and B. Goeldi, "A practical investigation of a high power, bidirectional charging system for electric vehicles," in *2014 16th European Conference on Power Electronics and Applications*, 26-28 Aug. 2014 2014, pp. 1-7, doi: 10.1109/EPE.2014.6910809.

[18]   J. H. Kim *et al.*, "Development of 1-MW Inductive Power Transfer System for a High-Speed Train," *IEEE Transactions on Industrial Electronics,* vol. 62, no. 10, pp. 6242-6250, 2015, doi: 10.1109/TIE.2015.2417122.

[19]   N. Shinohara, "Wireless power transmission progress for electric vehicle in Japan," in *2013 IEEE Radio and Wireless Symposium*, 20-23 Jan. 2013 2013, pp. 109-111, doi: 10.1109/RWS.2013.6486657.

[20]   M. Bojarski, E. Asa, K. Colak, and D. Czarkowski, "Analysis and Control of Multiphase Inductively Coupled Resonant Converter for Wireless Electric Vehicle Charger Applications," *IEEE Transactions on Transportation Electrification,* vol. 3, no. 2, pp. 312-320, 2017, doi: 10.1109/TTE.2016.2566921.

[21]   M. Bojarski, E. Asa, K. Colak, and D. Czarkowski, "A 25 kW industrial prototype wireless electric vehicle charger," in *2016 IEEE Applied Power Electronics Conference and Exposition (APEC)*, 20-24 March 2016 2016, pp. 1756-1761, doi: 10.1109/APEC.2016.7468105.

[22]   N. Toscani, M. Brunetti, M. S. Carmeli, F. Castelli Dezza, and M. Mauri, "Design of a Rotary Transformer for Installations on Large Shafts," *Applied Sciences,* vol. 12, no. 6, p. 2932, 2022.

[23]   Y. Zhang, J. Yang, D. Jiang, D. Li, and R. Qu, "Design, Manufacture, and Test of a Rotary Transformer for Contactless Power Transfer System," *IEEE Transactions on Magnetics,* vol. 58, no. 2, pp. 1-6, 2022, doi: 10.1109/TMAG.2021.3094135.

[24]   W. G. Hurley, W. H. Wolfle, and J. G. Breslin, "Optimized transformer design: inclusive of high-frequency effects," *IEEE Transactions on Power Electronics,* vol. 13, no. 4, pp. 651-659, 1998, doi: 10.1109/63.704133.

[25]   I. Villar, "Multiphysical Characterization of Medium-Frequency Power Electronic Transformers," EPFL, Lausanne, 2010.

[26]   Y. H. Sohn, B. H. Choi, E. S. Lee, G. C. Lim, G. H. Cho, and C. T. Rim, "General Unified Analyses of Two-Capacitor Inductive Power Transfer Systems: Equivalence of Current-Source SS and SP Compensations," *IEEE Transactions on Power Electronics,* vol. 30, no. 11, pp. 6030-6045, 2015, doi: 10.1109/TPEL.2015.2409734.

[27]   W. Chwei-Sen, G. A. Covic, and O. H. Stielau, "Power transfer capability and bifurcation phenomena of loosely coupled inductive power transfer systems," *IEEE Transactions on Industrial Electronics,* vol. 51, no. 1, pp. 148-157, 2004, doi: 10.1109/TIE.2003.822038.

[28]   Y. Cui, D. Wang, and A. Emadi, "Three-phase dual active bridge converter design considerations," in *IECON 2017 - 43rd Annual Conference of the IEEE Industrial Electronics Society*, 29 Oct.-1 Nov. 2017 2017, pp. 4696-4701, doi: 10.1109/IECON.2017.8216809.

[29]   R. T. Naayagi, A. J. Forsyth, and R. Shuttleworth, "High-Power Bidirectional DC–DC Converter for Aerospace Applications," *IEEE Transactions on Power Electronics,* vol. 27, no. 11, pp. 4366-4379, 2012, doi: 10.1109/TPEL.2012.2184771.

[30]   H.-j. Choi, W.-b. Lee, and J.-h. Jung, "Practical Controller Design of Three-Phase Dual Active Bridge Converter for Low Voltage DC Distribution System," *Electronics*, vol. 9, no. 12*,* doi: 10.3390/electronics9122101.

[31]   D.-D. Nguyen, N.-T. Bui, and K. Yukita, "Design and Optimization of Three-Phase Dual-Active-Bridge Converters for Electric Vehicle Charging Stations," *Energies*, vol. 13, no. 1*,* doi: 10.3390/en13010150.

[32]   D.-D. Nguyen, *Design of a 3-phase DAB converter for EV charging applications Outlines*. 2019.

[33]   O. A. Giddani, A. Y. M. Abbas, G. P. Adam, O. Anaya-Lara, and K. L. Lo, "Multi-task control for VSC–HVDC power and frequency control," *International Journal of Electrical Power & Energy Systems,* vol. 53, no. 0, pp.

[34]   R. Eriksson, "On the Centralized Nonlinear Control of HVDC Systems Using Lyapunov Theory,"
         Power Delivery, IEEE Transactions on, vol. 28, no. 2, pp. 1156-1163, 2013, doi:
         10.1109/tpwrd.2013.2240021.

Annex A: DAB converter parameters

The three-phase dual active bridge converter simulation parameters are listed below.

```
%% Parameters file for DAB_1MW3Ph_Thermal.slx
Fsw= 2e3;           % PWM switching frequency (Hz)
DT= 250e-9;         % Dead time (s)
Scope_Decimation=1; % Scope Decimation
Ts=1e-6;            % Control system sample time (s)
%
Pnom= 1000e3;          % Nominal power (W)
Vnom_HV= 1800;         % DC source 1 nominal voltage (V)
Vnom_LV= 1800;         % DC source 2 nominal voltage (V)
R_DCsrc1=1e-3;      % DC source 1 internal resistance (Ohm)
R_DCsrc2=40e-3;      % DC source 2 internal resistance (Ohm)m)
%
% Switches
Ron= 3.7500e-04;     % FET on-state resistance (Ohm)
Rs= 1e6;         % Snubber resistance Rs (Ohm) :
Cs= inf;         % Snubber capacitance Cs (F) :
Ron_Diode= 0.035e-3;   % Body diode resistance (Ohm)
Vf_Diode= 1.7;       % Body diode forward voltage drop (V)

% Coupling inductor
L_Inductor= 0.5e-9;  % Inductance (H)
R_Inductor= 1e-6;  % Resistance (Ohm)
%
C_Cap1=140e-6;
%R_Cap2=1e-6;
%C_Cap2=.5e-6;


% Transformer:
N_Tr= 1;           % Primary to secondary voltage ratio
Rprim_Tr=0.0113;     % Primary resistance (Ohm)
Lprim_Tr= 60e-6;   % Primary leakage inductance (H)
Rsec_Tr= 0.0120;     % Secondary resistance (Ohm
Lsec_Tr= 60e-6;        % Secondary leakage inductance (H)
Rm_Tr= 10e3;       % Magnetization resistance (Ohm)
Lm_Tr= 2.43e-3;     % Magnetization inductance (H)
%
% Filters
% High Voltage Capacitor:
C_HV= 100e-6;      % Capacitance (F)
RC_HV= 10e-3;        % Capacitor ESR (Ohm)
% Low Voltage Capacitor:
C_LV= 100e-6;     % Capacitance (F)
RC_LV= 10e-3;        % Capacitor ESR (Ohm)

%Thermal modeling parameters
Ts_Power=5e-6;
Ts_Control=50e-6;
IGBT_Rth_jc=0.028;% Changed for Semikron
IGBT_Cth_j=2.6804;
DIODE_Rth_jc=0.049;% Changed for Semikron
DIODE_Cth_j=1.3235;
Tj0=123;
Ad_IGBT=0.99996;
Bd_IGBT=[7.3151,0.37307];
Cd_IGBT=[4.9999e-06;9.8037e-05];
Dd_IGBT=[1.8288e-05,9.3268e-07;-19.607,1.8288e-05];
x0d=2.46e+07;
Ad_Diode=0.99996;
Bd_Diode=[7.4074,0.75556];
Cd_Diode=[4.9999e-06;4.9019e-05];
Dd_Diode=[1.8519e-05,1.8889e-06;-9.8037,1.8519e-05];
PulseDuration=5e-06;
DIODE_Tj_OnState=[25,125];
DIODE_If_OnState=[0 0.01 14 43 66.5 101 162 250 401 500];
DIODE_Vf_OnState=[0 0.75 1.13 1.4 1.53 1.65 1.81 2 2.25 2.39;0 0.5 0.9 1.2 1.37 1.55 1.81 2.11 2.5 2.71];
Vcc_Esw_Erec=[0,1800];
DIODE_If_Erec=[0 0.01 14 43 66.5 101 162 250 401 450 500];
DIODE_Tj_Erec=[25 125];
```

```
%Esw_On=[0 64.9129411764706 124.235294117647 246.917647058824 330 405.317647058824
499.270588235294 601.764705882353 713.576470588235 830.823529411765;0 83.6 160 318 425 522 643
775 919 1070];
%Esw_Off=[0 86.5333333333333 159.866666666667 279.4 330 398.2 456.133333333333 512.6
573.466666666667 631.4;0 118 218 381 450 543 622 699 782 861];
IGBT_Tj_Eoff=[25,125];
IGBT_Ic_Eoff=[0 37.8 99 199 250 300 349 400 451 499];
Vcc_Esw_Off=[0,1800];
Esw_Off=[0 86.5333333333333 159.866666666667 279.4 330 398.2 456.133333333333 512.6
573.466666666667 631.4;0 118 218 381 450 543 622 699 782 861];
Esw_On=[0 64.9129411764706 124.235294117647 246.917647058824 330 405.317647058824
499.270588235294 601.764705882353 713.576470588235 830.823529411765;0 83.6 160 318 425 522 643
775 919 1070];
IGBT_Tj_OnState=[25,125];
IGBT_Ic_Eon=[0 37.8 99 199 250 300 349 400 451 499];
IGBT_Ic_OnState=[0 1 16 77 131 174 276 375 500];
IGBT_Vce_OnState=[0 0.51 1 1.5 1.81 2.04 2.49 2.88 3.37;0 0.5 1 1.71 2.18 2.5 3.11 3.77
4.52]./3;
IGBT_Tj_OnState=[25 125];
Vcc_Esw_On=[0,1800];
IGBT_Tj_Eon=[25,125];
Ts_Simscape=5e-05;
Esw_Erec=[0 50.6196428571429 66.5892857142857 97.2321428571429 124.339285714286
146.142857142857 165 180.321428571429 191.517857142857 198 200.357142857143;0 85.9 113 165 211
248 280 306 325 336 340];
```